NASA-CR-201920

FINAL
IN-45-CR
OCIT

P427

68766

Final Report

on

Outgoing Spectral Radiance: A Climate Diagnostic

(Contract R.F. # NASW-4752)

Report No. 14

1 October 1992 - 31 March 1996

Prepared by

Shepard A. Clough
Michael J. Iacono

Atmospheric and Environmental Research, Inc.
840 Memorial Drive
Cambridge, MA 02139

Prepared for

National Aeronautics and Space Administration
2 Independance Square
300 E. Street, S.W.
Washington, D.C. 20546

PUBLICLY AVAILABLE

1) Introduction

This final report covers the work completed by AER for the project titled "Outgoing Spectral Radiance: A Climate Diagnostic". The following proposed tasks have been completed: 1) the acquisition and preparation of the IRIS-D spectral radiance database, 2) the validation of IRIS radiances with a line-by-line model, 3) the determination of a clear sky selection procedure, 4) an analysis of seasonal and regional spectral radiance means and variances for clear sky data, and 5) an examination of spectral radiance and emissivity for cloudy atmospheres including both thin cirrus and opaque clouds. Additional work includes the retrieval of seasonal variations of several atmospheric parameters related to climate variability from clear sky radiances over the tropical oceans. All of this work excluding the analysis of spectra containing clouds has been compiled into a paper which was completed during November, 1995 and submitted for review to JGR-Atmospheres in early December. A copy of the paper, "The Application of IRIS Clear Sky Spectral Radiances to Investigations of Climate Variability", authored by M. J. Iacono and S. A. Clough is included as Appendix A, and the topics discussed in detail in the paper are summarized below.

2) IRIS Spectral Radiance Dataset

The data utilized during this project consist of longwave spectral radiances measured by the IRIS-D Michelson interferometer aboard NIMBUS-4 over the ten month period from April, 1970 to January, 1971 (Hanel, et al., 1972). This dataset was obtained from R. Hanel at the National Space Science Data Center (NSSDC) in its original IBM binary format on 29 magnetic tapes. The radiances were extracted from this encoded and compressed format, converted to FORTRAN binary files, and stored on optical disks. IRIS-D measured outgoing radiances over the 400-1600 cm^{-1} spectral range with an unapodized resolution of 1.4 cm^{-1}. The sun-synchronous polar orbit of NIMBUS-4

allowed coverage of the globe twice per day, with equatorial crossings near local noon and midnight. The current database consists of approximately 700,000 individual spectra from all regions of the globe which represent about 55% of the possible number over the ten month observation period.

Our extensive use of the IRIS radiances revealed the presence of a significant number of spectra which clearly do not represent valid measurements of outgoing spectral radiance. Both flawed observations and Planck function calibration spectra are mixed into the dataset and number approximately 1% of the total. Subsequent analyses using this dataset would be compromised if these erroneous spectra are not considered, and they have been removed from the set of spectra included in this analysis. However, time did not permit the completion of the unanticipated task of extracting all erroneous spectra from the entire dataset.

3) IRIS Spectral Radiance Validation

Our initial emphasis was to assess the validity of using the IRIS radiances for climate related applications. To accomplish this, comparisons of individual measured IRIS radiance spectra with those calculated by a line-by-line radiative transfer model (LBLRTM) were performed. Radiosonde observations from the western Pacific island Guam for 1970 where obtained from NCAR (W. Spangler, private communication, 1995), and several were selected which temporally and spatially coincided with nearby clear sky radiance measurements from IRIS (e.g. Kunde, et al., 1974). The radiosonde profiles of temperature and relative humidity were used with LBLRTM to calculate radiance spectra, and differences between the measured and calculated spectra were examined. A numerical correction was applied to account for the effect of the instrument field of view by convolving the calculated spectra with a spectrally varying rectangular window. Additional corrections were used to simulate the spectral variation of ocean emissivity and reflectivity. Radiance residuals were generally less than 3 (mW m^{-2} sr^{-1})/cm^{-1} across the longwave

spectral range, showing good agreement between the theoretical and measured radiances despite the remaining sources of error.

Among the errors which contribute to the radiance residuals, the largest was found to result from inaccuracies in the radiosonde measurement of temperature and water vapor profiles during this period. Radiosondes in use from 1965 to the early 1970s produced negative relative humidity errors of more than 20% during daytime soundings, due to sunlight artificially warming the humidity sensor (Elliot and Gaffen, 1991). This error is shown to contribute as much as 5 (mW m^{-2} sr^{-1})/cm^{-1} to the radiance residual in the infrared window region by examining measured and calculated radiance differences for successive daytime and nighttime observations from the same location. Other errors are introduced by limitations in defining both the temperature profile and the profiles of trace gases such as ozone and methane. It is apparent from this analysis that the accurate specification of atmospheric parameters is of critical importance to validating future spectral radiance measurements.

4) Clear Sky Seasonal and Regional Mean Spectral Radiance

Several geographic regions were defined to examine clear sky spectral radiances over seasonal time periods. These include four equatorial ocean areas and two northern mid-latitude ocean areas. A portion of the Sahara Desert was also included to investigate the effect of a relatively homogeneous land area on outgoing spectral radiance. An analysis of clear sky radiances requires a method of separating clear sky spectra from those affected by cloudiness, and several were examined. A threshold technique, in which spectra are separated based on the brightness temperature at a specific frequency provides a sufficient level of distinction to isolate the clearest cases from a group of observed spectra. Distributions of brightness temperature at 1128 cm^{-1} were used to determine an appropriate threshold for each season and region. These also illustrate the relative frequencies of clear

and cloudy spectra for the various seasons and regions which are consistent with observed climatological patterns.

Seasonal means and standard deviations of spectral radiance and brightness temperature were analyzed for each region. The seasonal mean spectral radiances show only small differences over the tropical oceans due to the relatively uniform sea surface temperatures (SSTs) and atmospheric conditions in the tropics, though these differences result from a combination of variations in ocean temperature, atmospheric temperature, and water vapor profiles. Standard deviations of spectral brightness temperature are as low as 1 K in the main CO_2 absorption band from 580-750 cm^{-1}, which indicates the remarkable stability and reliability of the dataset on a seasonal time scale. Standard deviations are generally 1-2 K across the 800-1200 cm^{-1} infrared window for the tropical regions, which is consistent with the variability of ocean temperature near the equator. The shape of the spectral brightness temperature standard deviations are shown to be effective at illustrating the relative variability between the background surface emissions and those from the intervening atmosphere. Mean brightness temperature spectra from the northern mid-latitude oceans display not only the expected seasonal variations related to SST changes, but also the greater variability of ozone during the winter months due to the diminished ozone production and increased transport.

5) Clear Sky Spectral Radiance Retrievals

A linear retrieval algorithm has been used to quantify the seasonal surface and atmospheric changes that would be necessary to produce the observed seasonal spectral radiance differences for the tropics. The retrieval makes use of all the tropospheric spectral information contained in the IRIS radiances from 430-1200 cm^{-1}, and interprets seasonal minus annual mean radiance differences as simultaneous changes in SST, tropospheric temperature, and water column amounts, as well as water and temperature lapse rates. The

low standard deviations of spectral radiance support this single layer tropospheric retrieval on the assumption that the individual spectra are similar to the mean spectrum.

In most cases the retrieved seasonal minus annual mean SST difference needed to account for the seasonal differences in IRIS mean radiance agrees with the observed SST changes within 0.7 K. Tropical ocean temperatures generally decreased throughout this ten month period due to the La Nina conditions which developed during 1970. In addition, the retrieved tropospheric layer temperatures, water column amounts and lapse rates are consistent with the SST variations. Water column seasonal variations on the order of 5-10 percent occur over the equatorial Pacific and Atlantic regions for this annual cycle. Over the Indian Ocean water column changes of 10-20 percent occur in response to the stronger than normal summer 1970 Indian monsoon circulation.

6) Cloudy Sky Spectral Radiance and Emissivity

To conclude the project, we conducted a brief analysis of the cloudy spectra that were not considered earlier, though this part of the study was limited to the tropical ocean regions. Since partial cloudiness cannot be identified from individual radiance spectra, no distinction is made between partially cloud-filled fields of view, which will include emission from the surface, and those that are totally cloud filled. Of specific interest are the distinct properties of spectral radiance and emissivity for ice and water clouds, and it is presumed that, for non-clear conditions, a single cloud type dominates any given field of view, although this is not necessarily the case. Once clear spectra have been removed using the brightness temperature thresholds discussed above, the remaining spectra are grouped according to their brightness temperature (BT) and their individual spectral properties. Two height levels at 3 km and 7 km were used to classify cloudy spectra into low, middle, and high categories. These heights correspond to temperatures near 285 K and 260 K in the mean tropical profile. Cloudy spectra are then separated based on their BT at 1128 cm^{-1}, which is taken to be an effective cloud top temperature for cases where

the cloud is sufficiently opaque. Thus, high cloud spectra have an 1128 cm^{-1} BT colder than 260 K, middle cloud spectra between 260 K and 285 K, and low cloud spectra between 285 K and the previously defined clear sky BT threshold (usually between 292 K and 295 K in the tropics).

A further distinction is used to separate cloudy spectra according to their composition (liquid water or ice) based on their spectral properties. A multi-spectral technique developed by Ackerman, et al. (1990) has been used to distinguish ice cloud from water cloud. In this approach, mean brightness temperatures are computed for three narrow bands: 8.3-8.4 microns, 11.06-11.25 microns, and 11.93-12.06 microns. Due to the difference in spectral properties of ice and water, the BT difference between 8 and 11 microns is generally larger than the BT difference between 11 and 12 microns for ice clouds, while the reverse is true for water clouds. Using this distinction, the low/warm cloud category is divided into two groups that represent a) low water clouds and b) high ice clouds which are presumed to be sufficiently thin to transmit radiance from the warmer atmosphere below. Similarly, the middle level cloudy spectra are separated into water and ice categories. The mid-level ice category may also contain partially thin high clouds which appear warm enough to fall into this group. The high/cold spectra are all presumed to indicate the presence of opaque ice clouds.

Figure 1 is a scatter plot of the 11-12 micron BT difference as a function of the 8-11 micron BT difference for all 626 IRIS spectra observed over the equatorial Western Pacific during September, 1970. The spectra are separated into the categories mentioned above, with each group plotted in a different color as shown on the plot. As discussed in Ackerman, et al., (1990), clear spectra generally have negative 8-11 BT differences (below the solid black line), and this agrees well with the approach taken in this work which is to identify clear spectra based on a BT threshold at 1128 cm^{-1}. A threshold of 294 K produces the group plotted in red, most of which appear below the black line. Spectra containing ice clouds, however, typically have large positive 8-11 BT differences which are

greater than the 11-12 BT difference. These are plotted in dark blue (opaque high clouds), light blue (mid-level ice clouds), and magenta (thin high clouds), and they appear above the dotted line. Spectra containing water clouds have larger 11-12 BT differences and appear between the solid and dotted lines. These are plotted in green for mid-level water clouds and yellow for low level water clouds. There is considerable overlap between the clear and low-level water groups which is primarily due to partial cloudiness.

The methods of separation defined above have been applied to both the Western and Eastern equatorial Pacific Ocean regions for each of the four seasons. The total number of spectra for each season and the number that occur within the clear and cloud categories are listed in Table 1 for the Western Pacific region and in Table 2 for the Eastern Pacific region. In general, the number of clear spectra represent the largest group varying from 35 to 60 percent of the total number of spectra. This can be only loosely interpreted as a clear sky frequency due to limitations in temporal and spatial averaging, though the percentages

Table 1: The number of radiance spectra for each season over the equatorial Western Pacific for total, clear, and five cloud categories. An 'X' in the season abbreviation indicates missing data for that month.

	XAM, 1970	JJA, 1970	SON, 1970	DJX, 1970-71
TOTAL	1566	2332	2177	854
CLEAR	569	1181	1288	462
THICK CI	137	133	48	41
THIN CI	98	96	72	27
MID ICE	252	304	140	100
MID WATER	82	59	28	27
LOW WATER	428	559	601	197

are consistent with satellite observed clear sky fractions (Rossow, 1993). Note the relative frequency of thick cirrus clouds is substantially lower in the Eastern Pacific than in the west for all seasons, which is also in agreement with observations. Thin cirrus occur more frequently in the west during spring and fall. Mid-level ice clouds are much more frequent in the west, and since this category likely includes thin, high cirrus at intermediate levels of

Table 2: The number of radiance spectra for each season over the equatorial Eastern Pacific for total, clear, and five cloud categories. An 'X' in the season abbreviation indicates missing data for that month.

	XAM, 1970	JJA, 1970	SON, 1970	DJX, 1970-71
TOTAL	1505	2350	2166	881
CLEAR	762	1112	994	327
THICK CI	42	9	1	25
THIN CI	27	115	41	23
MID ICE	96	64	56	47
MID WATER	68	91	181	68
LOW WATER	510	959	893	391

opacity, the frequency of thin cirrus is probably much higher in the west than that indicated by the 'THIN CI' category. Prabhakara et al., (1993) have previously identified this tendency. Mid and low level water clouds are more apparent from these data over the Eastern Pacific during 1970, largely due to the lower frequency of obscuring high cloud in this region.

The mean spectral emissivity has been examined for each of the cloud categories. Radiance spectra are converted to an effective emissivity by dividing each radiance spectrum by the Planck function at the 1128 cm^{-1} brightness temperature of each spectrum.

Means and standard deviations are then calculated for the groups of spectra defined above. These are plotted in Figure 2 for the summer (June, July, August) 1970 season over the Western Pacific and in Figure 3 for the summer 1970 season over the Eastern Pacific. The color codes for each spectra category are the same as in Figure 1. Since these spectral emissivities are relative to the Planck function at 1128 cm^{-1}, the emissivity at 1128 cm^{-1} will always be one and the standard deviation at 1128 cm^{-1} will always be zero. The warmest and clearest spectra tend to have the highest emissivity in the 770-950 cm^{-1} window region. Spectra containing water cloud have lower emissivity in this range, while the colder spectra containing ice cloud have even lower emissivities and display greater spectral variation over this range. This is a consequence of the spectral variation in absorptive properties of water and ice. In the 1080-1250 cm^{-1} spectral range there is much less variation in spectral emissivity among the categories due to the much lower variation in water and ice absorptivity in this wavenumber range. At all other frequencies, the presence of opaque ice cloud results in a higher emissivity than the other cloud categories. In addition, high cloud produces a higher standard deviation of spectral emissivity due to the variation of cloud temperatures and ice particle properties. Finally, the emissivity standard deviation is much higher in the CO_2 (580-750 cm^{-1}) and O_3 (1000-1080 cm^{-1}) regions for opaque ice cloud spectra since the 1128 cm^{-1} BT on which the emissivity is based varies more extremely for this category than the others. In fact the 1128 cm^{-1} BT can take a value either above or below the mean CO_2 and O_3 emission temperatures depending on the level and opacity of the high cloud.

7) Recommendations

We have shown that clear sky spectral radiances provide substantial information on the atmospheric state that could not be derived from integrated quantities. They are of considerable use in identifying absorptive effects from individual molecular species and specifying both the surface and tropospheric temperatures. Seasonal mean spectral radiance

differences reflect observed seasonal variations in surface temperature, atmospheric temperature up to the stratosphere, and water vapor column amount. They would therefore be of significant use in validating general circulation model longwave radiative simulations. The retrieval techniques described could be used to obtain sea surface temperature and water column amounts from individual spectra over larger areas and longer time periods than those considered here. In addition, the intraseasonal variability of spectral radiance or brightness temperature provides information on variations of surface and atmospheric properties and of individual molecular species such as ozone. Our use of the IRIS-D spectral radiance dataset has demonstrated the impressive quality of these data, and we strongly encourage both their use in future projects related to atmospheric variability and also the development of future instruments to measure longwave spectral radiance as an effective way of monitoring the global climate system.

8) References

Ackerman, S. A., W. L. Smith, J. D. Spinhirne, and H. E. Rivercomb, The 27-28 October, 1986 FIRE IFO cirrus case study: spectral properties of cirrus clouds in the 8-12 micron window, Mon. Wea. Rev., 118, 2377-2388, 1990.

Elliot, W. P. and D. J. Gaffen, On the utility of radiosonde humidity archives for climate studies, Bull. Amer. Meteorol. Soc., 72, 1507-1520, 1991.

Hanel, R. A., B. J. Conrath, V. G. Kunde, C. Prabhakara, I. Revah, V. V. Salomonson, and G. Wolford, The Nimbus 4 infrared spectroscopy experiment 1: calibrated thermal emission spectra, J. Geophys. Res., 77, 2629-2641, 1972.

Kunde, V. G., B. J. Conrath, R. A. Hanel, W. C. Maguire, C. Prabhakara, and V. V. Salomonson, The Nimbus 4 infrared spectroscopy experiment 2: comparison of observed and theoretical radiances from 425-1450 cm-1, J. Geophys. Res., 79, 777-784, 1974.

Prabhakara, C., D. P. Kratz, J.-M. Yoo, G. Dalu, and A. Vernekar, Optically thin cirrus clouds: radiative impact on the warm pool, J. Quant. Spectrosc. Radiat. Transfer, 49, 467-483, 1993.

Rossow, W., Clouds, in Atlas of Satellite Observations Related to Global Change, edited by R. J. Gurney, J. L. Foster, and C. L. Parkinson, pp. 141-163, Cambridge Univ. Press, New York, 1993.

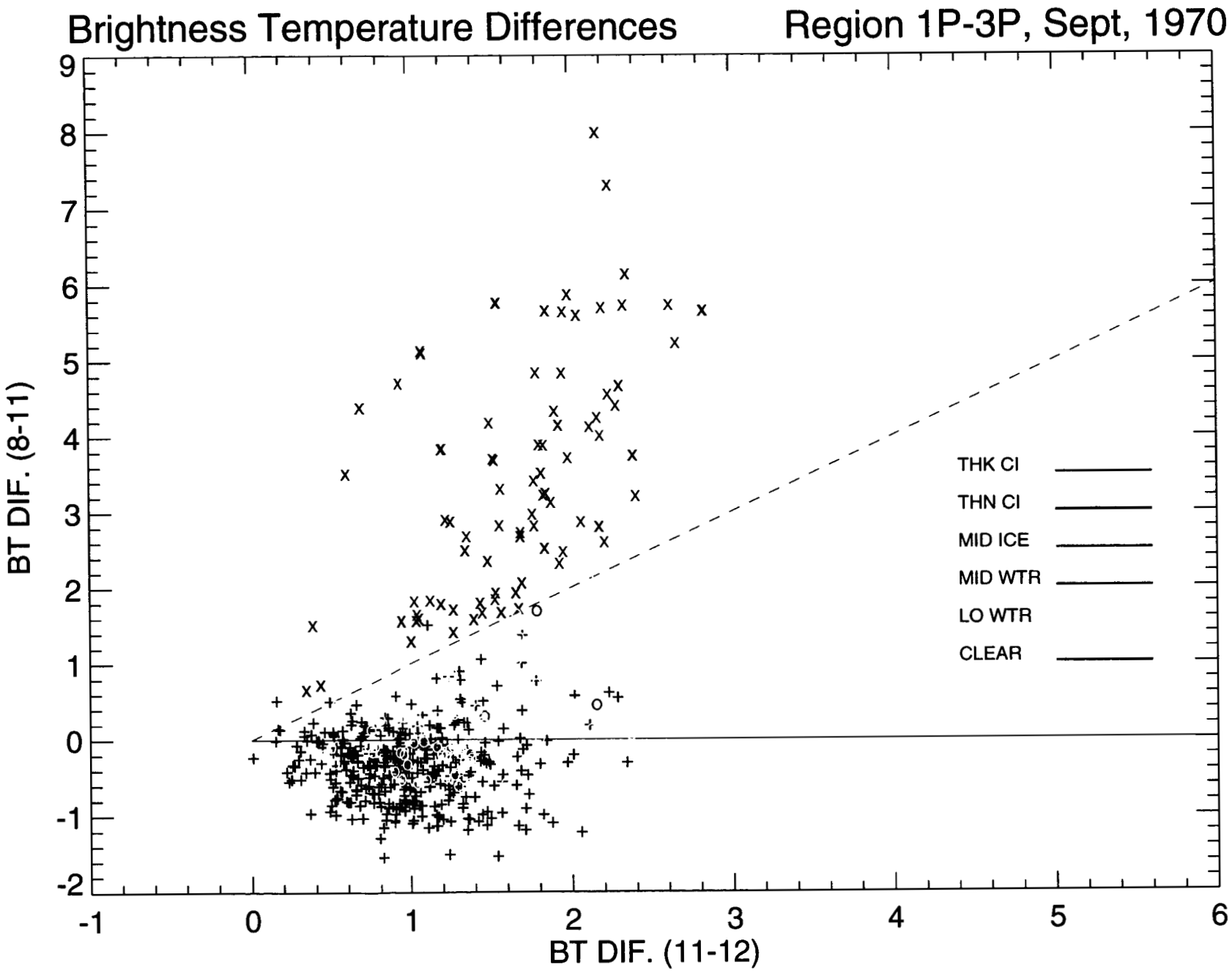

FIGURE 1

25 Mar 96 15:42

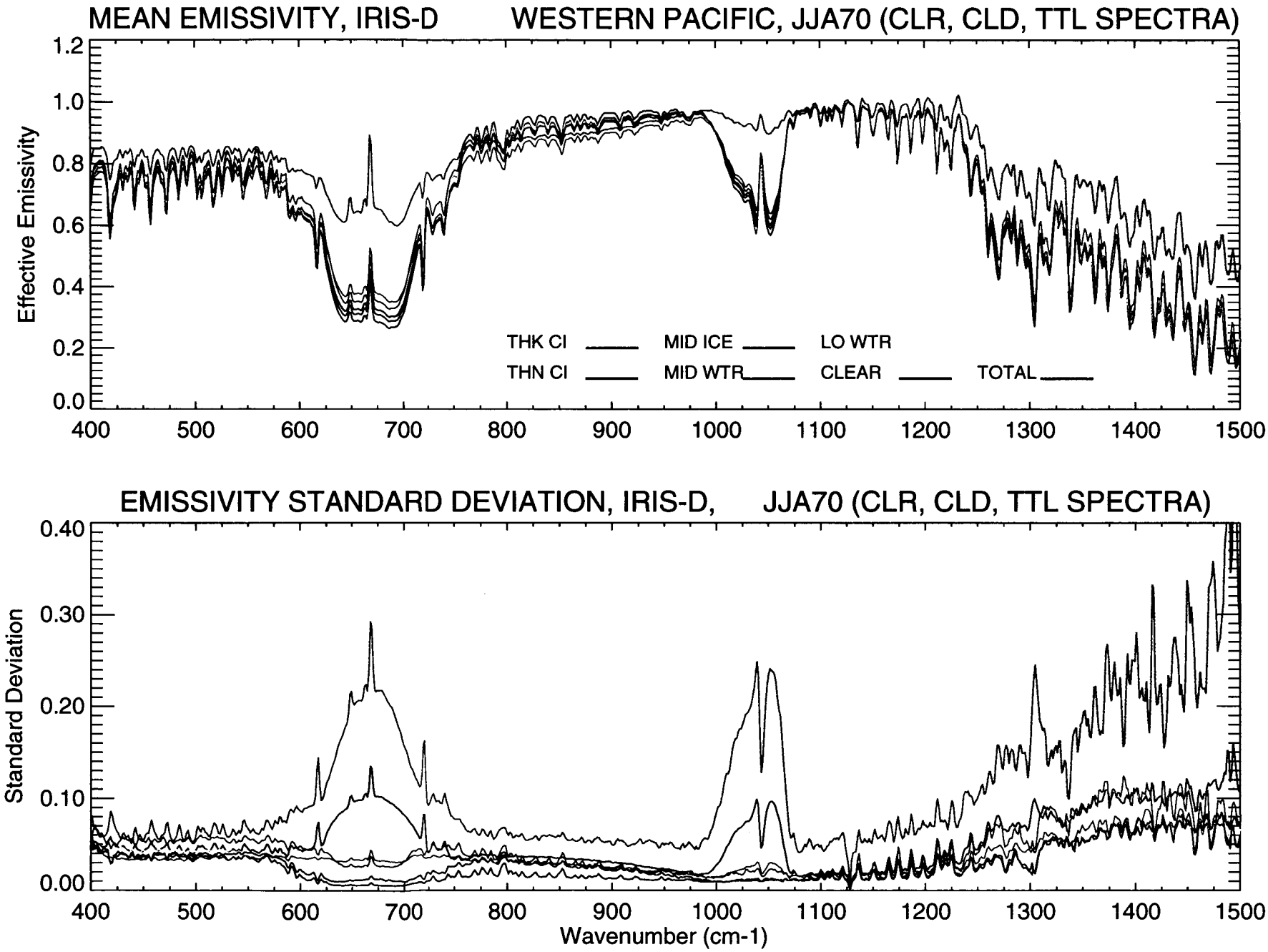
MEAN EMISSIVITY, IRIS-D
WESTERN PACIFIC, JJA70 (CLR, CLD, TTL SPECTRA)
Effective Emissivity
THK CI
MID ICE
LO WTR
THN CI
MID WTR
CLEAR
TOTAL
EMISSIVITY STANDARD DEVIATION, IRIS-D,
JJA70 (CLR, CLD, TTL SPECTRA)
Standard Deviation
Wavenumber (cm-1)

FIGURE 2

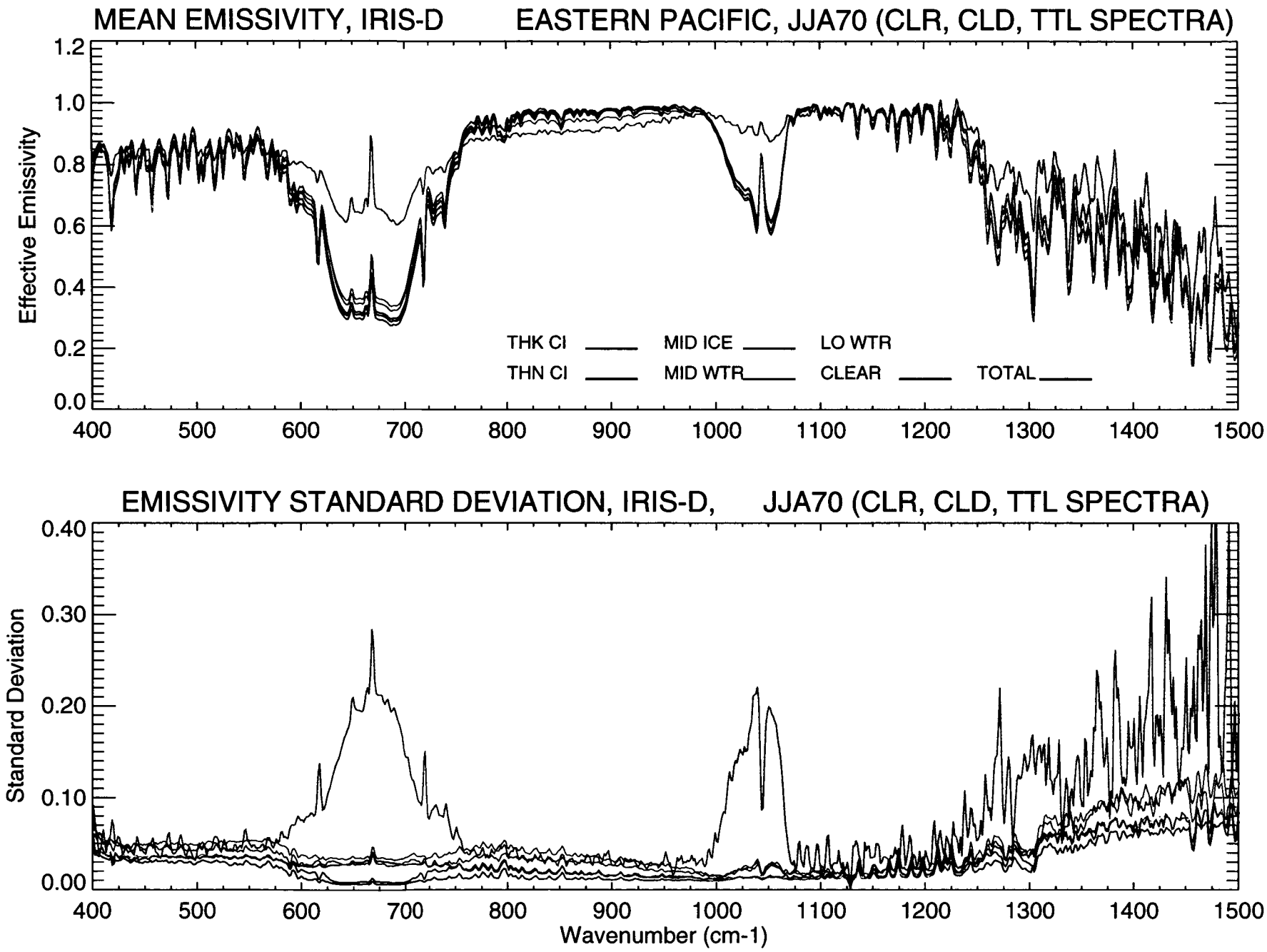
MEAN EMISSIVITY, IRIS-D
EASTERN PACIFIC, JJA70 (CLR, CLD, TTL SPECTRA)
Effective Emissivity
1.2
1.0
0.8
0.6
0.4
0.2
0.0
THK CI
MID ICE
LO WTR
THN CI
MID WTR
CLEAR
TOTAL
400
500
600
700
800
900
1000
1100
1200
1300
1400
1500
EMISSIVITY STANDARD DEVIATION, IRIS-D,
JJA70 (CLR, CLD, TTL SPECTRA)
Standard Deviation
0.40
0.30
0.20
0.10
0.00
Wavenumber (cm-1)

FIGURE 3

APPENDIX A

The Application of IRIS Clear Sky Spectral Radiance to Investigations of Climate Variability

Michael J. Iacono and Shepard A. Clough
Atmospheric and Environmental Research, Inc., Cambridge, MA

Short title: Spectral Radiance and Climate Variability

Abstract

An investigation of clear sky spectral radiances and their applicability as a diagnostic for climate variability is described. Global observations of outgoing longwave radiation during 1970 from the Infrared Interferometer Spectrometer (IRIS) aboard Nimbus 4 cover nearly a full annual cycle, and the spectral content of the data provides unique information for examining regional and seasonal variations of spectral radiance. The IRIS radiances have been validated against a line-by-line radiative transfer model (LBLRTM) and are found to compare favorably with calculated radiances. A brightness temperature threshold technique is used to separate clear and cloudy spectra, and seasonal means of clear sky spectra are analyzed for tropical and northern mid-latitude ocean areas. Brightness temperature standard deviations are also examined spectrally. Values of 1-2 K in the tropics and 2-3 K at mid-latitudes in the 800-1200 cm^{-1} window region are consistent with observed ocean temperature variability. Spectral features in the standard deviations reflect the variation of surface temperature, tropospheric temperature, and water vapor in the tropics and the increased variability of ozone during winter in the northern hemisphere. Spectral differences between seasonal and annual mean outgoing radiance are associated with variations in atmospheric parameters, and a linear retrieval algorithm is used to quantify these changes in the tropics. Retrieved seasonal sea surface temperature (SST) differences are typically within 0.7 K of the observed SST differences. Interseasonal water column variations during this annual cycle are 5-10% over the tropical Pacific and Atlantic and 10-20% over the equatorial Indian Ocean. In general, the retrieved seasonal changes in temperature and water vapor parameters are consistent with the known conditions of the 1970 tropical ocean and atmosphere. These variations are detectable as signatures in outgoing spectral radiances and provide significant information relevant to climate change.

1. Introduction

The global balance at the top of the atmosphere between the absorbed solar radiation and the outgoing longwave radiation as measured from space significantly controls the earth's climate system. The response of both components of this radiative equilibrium to global forcings must be simulated accurately for climate model predictions to be valid. A greater understanding of the connection between the spectral content of outgoing radiance and climate change is essential to the validation of climate models. This study presents an analysis of clear sky, longwave, spectral radiances and assesses their applicability as a diagnostic for climate change simulations. The relation between cloudy spectral radiances and climate variability will be the topic of a subsequent paper.

Spectral radiances have the virtue of providing significantly more information on the atmospheric state than do integrated quantities. With a resolution on the order of 1 cm^{-1}, individual chemical species can be distinguished and complex temperature effects can be detected. Clear sky infrared spectra contain radiative contributions from the surface and all atmospheric levels and represent a detailed fingerprint of the atmospheric state that is sensitive to climate changes. For example, the vertical and spectral variation of longwave water vapor emissions [Clough and Iacono, 1995] can provide important evidence toward resolving the magnitude and vertical distribution of water vapor feedbacks resulting from climate change [Sinha and Harries, 1995]. An analysis of regional and temporal mean radiances over a large portion of the infrared spectrum will demonstrate the extent to which climate processes are detectable as spectral signatures in the outgoing radiance.

Many observational programs have improved our understanding of the earth's radiation budget and the vertical structure and composition of the atmosphere. The Earth Radiation Budget Experiment (ERBE) has produced the most comprehensive, integrated measurements of the three components of earth's radiation budget that are measured from space: incident solar irradiance, reflected shortwave radiation, and emitted longwave radiation [Harrison, et al., 1993]. Other instruments, such as the High Resolution Infrared

Radiation Sounder (HIRS), have been remotely sensing the atmosphere from NOAA satellites since the 1970's [Susskind, 1993]. These observations have concentrated on spectrally integrated quantities or have been constrained to a selected number of spectral intervals or channels. Only a few orbiting experiments to date have provided global measurements of outgoing longwave radiation over a wide portion of the infrared spectrum. These include the Soviet METEOR program from the late 1970's, which carried three Fourier spectrometers into orbit to measure spectral radiance at 5 cm^{-1} resolution over the 400-1600 cm^{-1} region [Spankuch and Dohler, 1985], and the IRIS (Infrared Interferometer Spectrometer) instrument aboard the polar-orbiting Nimbus 4 satellite [Hanel, et al., 1972]. The IRIS dataset, which has been applied to the current study, consists of global measurements of outgoing spectral radiance over the 400-1600 cm^{-1} range (6.25-25 μm) at an unapodized spectral resolution of 1.4 cm^{-1} for the ten-month period from April, 1970 to January, 1971. Future programs including the Atmospheric Infrared Sounder (AIRS) planned for the Earth Observing System (EOS) PM-1 satellite will improve both the resolution and temporal extent of spectral radiance observations, and the current work should be interpreted as an example of the potential utility of these measurements.

Several studies have made use of the IRIS dataset to validate spectral radiative transfer models, to examine atmospheric constituents, and to quantify the seasonal variation of thin cirrus [e.g. Kunde, et al., 1974; Prabhakara, et al., 1993]. In addition, the split window technique for determining sea surface temperature from outgoing radiance, which uses two spectral intervals in the infrared window to account for the lower tropospheric water vapor absorption, was developed with this dataset [Prabhakara, et al., 1974].

The initial aspect of this work pertains to the development of an archive of quality controlled IRIS radiance spectra and to an analysis and validation of selected observations against line-by-line calculated radiances. These test cases involve comparing satellite observed spectra with those derived from calculations based on soundings of temperature

and water vapor profiles for both tropical and mid-latitude locations. The application of a correction to the calculated spectrum to account for the instrument field of view produces significantly reduced spectral residuals. The dataset and a tropical validation are discussed in further detail in section 2.

The relationship between outgoing spectral radiance and climate variations is explored by examining seasonal mean, clear sky radiance spectra over several geographic areas. Cloud clearing is accomplished with the application of a brightness temperature threshold in the spectral window region. Spectra from tropical Pacific, Atlantic, and Indian Ocean areas have been examined, and spectra from the Northern Pacific and Atlantic Oceans have been included to provide a non-tropical perspective to the analysis. In addition, radiance spectra from the Sahara Desert have been analyzed to study the effect of a relatively homogenous land surface on the outgoing longwave radiation. The mean spectral radiances, their standard deviations, and their relevance to the interseasonal climate variability during 1970 are presented in section 3.

Satellite measured radiances at selected frequencies or over integrated bands have been used to quantify many important properties of the earth and its atmosphere. For example, outgoing infrared radiances have been used to estimate sea surface temperatures to accuracies of 1-2 K [e.g. Strong and McClain, 1984] by using two or more spectral intervals to account for the error induced by the tropospheric water vapor absorption and emission. Taking advantage of all the tropospheric spectral information contained in the IRIS radiances from 430-1200 cm^{-1}, a retrieval algorithm has been applied to differences between seasonal mean and ten-month mean spectral radiances in the tropics. This retrieval interprets the seasonal mean radiance differences as changes in sea surface temperature, tropospheric temperature, and water column amount, as well as water and temperature lapse rates and quantifies their interseasonal variations. Data from part of the water vapor pure rotation band (430-600 cm^{-1}) are included, since this region provides important radiative information on the middle and upper tropospheric water vapor and plays a critical

role in the evolution of greenhouse warming [Sinha and Harries, 1995]. Section 4 provides a discussion of the retrieval code and the results for the tropical ocean regions.

2. IRIS Spectral Radiance Validation

2.1. IRIS Dataset

The IRIS-D Michelson interferometer aboard Nimbus 4 provided improved performance and spectral resolution over its Nimbus 3 predecessor, IRIS-B [Hanel, et al., 1971]. In operation from April, 1970 to January, 1971, IRIS-D measured outgoing longwave radiance over the 400-1600 cm^{-1} range (6.25-25 μm) at a nominal, unapodized spectral resolution of 1.4 cm^{-1}. Since the satellite was sun-synchronous, it covered the globe twice per day, with equatorial crossings near local noon and midnight. The diameter of the circular viewing area was approximately 94 km at the satellite's mean altitude of 1100 km, and the cycle time of the interferometer allowed measurements at intervals of 16 seconds. The current database, provided by the National Space Science Data Center (NSSDC), consists of nearly 700,000 individual spectra representing about 55% of the possible number over the ten-month period.

The IRIS data selected for analysis have been processed to filter out spurious radiance spectra that were clearly not representative of actual or spectrally complete observations. Many spectra were found to be Planck function calibration spectra, and in some instances they were numerous enough to contaminate the subsequent analysis if not carefully removed. The low standard deviation of the spectra in the CO_2 absorption band (presented in section 3.2) allows the identification of erroneous spectra based on their variation at the 667 cm^{-1} center of this band. All selected spectral radiances were also examined visually, and the obviously defective spectra were discarded. In addition, numerous spectra from January, 1971, although apparently valid, were geographically misidentified and were also excluded.

2.2. Tropical Pacific Radiance Validation

In order to assess the validity of using IRIS radiances for climate related applications it is necessary to establish the data quality. Comparisons of individual measured IRIS radiance spectra with those calculated by a line-by-line radiative transfer model (LBLRTM) [e.g., Clough and Iacono, 1995] using identical profiles of temperature, water vapor, and other atmospheric constituents have been performed similar to those of Kunde, et al. [1974]. An IRIS radiance spectrum observed near Guam in the Western Pacific at 0202 UT on 27 April, 1970 was selected since a routine radiosonde measurement taken from Guam two hours earlier at 0000 UT represents a typical tropical profile over the ocean during nominally clear sky conditions close to local noon. Standard tropical atmospheric profiles of temperature and water vapor [Anderson, et al., 1986] were used above the sounding levels to extend the measured profiles to higher altitudes as shown in Figure 1. The small discontinuities in the temperature curve (Figure 1a) near 26 km and in the water vapor curve (Figure 1b) near 10 km, where the observed data and the standard profiles are joined, are considered acceptably small. The temperature discontinuities near 24 km and in the lower troposphere were part of the observed sounding and were left unchanged. The spike in the moisture profile at 4.5 km, or 600 mb, represents an increase in relative humidity from 15 to 45 percent at 277 K and may indicate the presence of partial mid-level cloud. This is consistent with the spectra observed east of the island during this time, which display the cold brightness temperatures indicative of cloudiness. The IRIS spectrum selected for the validation represents an area centered 170 km north of Guam, and though generally clear, may contain partial cloud traces from the cloud deck to the south.

The profiles of Figure 1 were used with the line-by-line model to calculate a radiance spectrum from 400-1600 cm^{-1}. The Hamming scanning function was applied to this spectrum which is consistent with the apodization function used to convert the measured interferogram from Fourier space to the frequency domain. The maximum optical path difference for the Nimbus 4 interferometer of 0.36 cm was used in the application of the Hamming scanning function to the computed radiance. The calculated (LBL) and

measured (IRIS) spectra for this case are shown in Figure 2a. For reference, the blackbody Planck functions at several appropriate temperatures are included. The strongest absorption from water vapor lines and continuum is apparent in the H_2O pure rotation band below 580 cm^{-1}, where it most significantly influences atmospheric longwave fluxes and cooling rates [Clough and Iacono, 1995], and in the H_2O vibration-rotation band above 1200 cm^{-1}. Weaker H_2O absorption is also apparent across the 800-1200 cm^{-1} window region. Other prominent absorption features include the main band of carbon dioxide from 580-750 cm^{-1} centered at the 667 cm^{-1} Q-branch, ozone from 980-1080 cm^{-1}, methane from 1190-1370 cm^{-1}, and nitrous oxide from 1150-1320 cm^{-1}. These features are indicated in Figure 2a. The coldest brightness temperatures (near 215 K) occur in the P and R branches of the CO_2 band, where the atmosphere is opaque in the lower troposphere and the radiation emanates close to the tropopause. The central spike at 667 cm^{-1} is the frequency of greatest CO_2 opacity and thus represents mean radiation emanating from the warmer stratosphere. The coldest measured brightness temperatures of about 260 K in the partially opaque ozone band include radiation from both the surface and the stratosphere. The central peak at 1043 cm^{-1} is at the band center of the strong ozone absorption and reflects a larger contribution from the surface radiance. The warmest brightness temperatures in both spectra are close to 298 K at 1127.7 cm^{-1} and are several degrees cooler than the local 301.2 K sea surface temperature derived from analyzed ship observations [Kunde, et al., 1974].

Several numerical corrections have been applied to the calculated radiance. First, the effect of the instrument field of view on the spectral radiance is accounted for by convolving the calculated spectrum with a varying rectangular window with the center frequency given by

$$v' = v\,(1 + b^2/4) \tag{1}$$

and the width of the window given by

$$\Delta v' = v\,(b^2/2) \tag{2}$$

where v is the wavenumber value associated with the central ray of the interferometer and defines the left edge of the window, and b (equal to 0.04363 for IRIS-D) is the half angle of the instrument's field of view in radians [Bell, 1972]. Additional corrections account for the effects of the spectral variation of ocean emissivity and the radiance reflected from the ocean surface. The sea water emissivity calculations of Masuda, et al., [1988] for a low zenith angle and low wind speed have been utilized in the LBLRTM calculation for the Guam case. Outgoing longwave contributions from the reflected atmosphere have also been implemented following the measurements of Smith, et al., [1995].

The calculated minus observed (IRIS - LBL) radiance difference for the Guam case incorporating these corrections is illustrated in Figure 2b. The field of view correction substantially reduces sharp oscillations in the difference at the centers of the strongest absorption lines, especially at the peaks of the CO_2 and O_3 bands. The largest errors tend to occur at both ends of the spectrum near the spectral limits of the interferometer. Contributions from the emissivity and reflected atmosphere are small for this case, but produce a slight reduction in the slope of the residual through the 700-1000 cm^{-1} range. Comparison with Figure 5 of Kunde, [1974] demonstrates a noticeable improvement in the residual. Overall, the radiance error is generally less than 3 (mW m^{-2} sr^{-1})/cm^{-1} or, in terms of brightness temperature, the line-by-line calculated excess in the 800-1000 cm^{-1} region is on the order of 2 K.

Several known errors contribute to the residual in Figure 2b. Inadequate measurement of the temperature and water vapor profiles used in the calculation is particularly significant, due to the errors associated with radiosonde measurements from this period. The radiosonde housing in use from 1965 to the early 1970's allowed sunlight to warm the relative humidity sensor above the ambient temperature during daytime soundings, causing large negative errors in the observed relative humidity of more than 20% (Elliott and Gaffen, 1991). Two additional Guam clear sky cases (one daytime and one nighttime) were selected to demonstrate the contribution of this error to the outgoing

radiance. Figure 2c shows the IRIS-LBL spectral radiance difference between a calculation based on radiosonde data from 12 July, 1970 at 1200 UT (10 PM local time) and an IRIS spectrum taken two hours later over an area centered 65 km east-southeast of the island. Figure 2d shows the IRIS-LBL difference using the 13 July, 1970 at 0000 UT (10 AM local time) radiosonde profiles and an IRIS spectrum observed two hours later and centered 65 km south-southwest of the island. Both the field of view and emissivity corrections were applied to the calculations. The larger residual in the daytime case across most of the 450-1250 cm^{-1} range is primarily due to the diurnal relative humidity error. The residual in Figure 2b was also derived from a calculation using a daytime sounding and would also include this substantial error. An additional relative humidity error involving the thermal lag of the hygristor sensor contributes a further deficit of as much as 5% in both night and day soundings, and this would account for part of the residual in Figures 2b-2d. The difference in all three cases in the main CO_2 band, where radiation emanates from the lower stratosphere, corresponds to 3-4 K errors in brightness temperature. This is a result of either an error in the temperature measurement above the tropopause or in the use of the standard profiles above 26 km. Specification of the sea surface temperature is another source of uncertainty. In addition, the unspecified presence of thin or partial cloud discussed earlier may contribute to the residual in the 400-1000 cm^{-1} region in Figure 2b as evidenced by the spectral variation in absorptive properties of water and ice clouds [e.g. Ackerman, et al., 1990]. Differences in the ozone and methane bands are indicative of deviations between the actual profiles of these molecules and the climatological amounts used in the model. Finally, these residuals illustrate the limitation on quantifying the IRIS instrument's accuracy introduced by uncertainties in defining the atmosphere. The importance of accurate atmospheric specification to validating future spectral radiance instruments such as AIRS cannot be overstated.

3. Seasonal and Regional Mean Spectral Radiance

The previous section demonstrated that individual IRIS outgoing radiance spectra are sufficiently accurate to compare favorably with line-by-line calculations within the discussed limitations and to represent realistically various radiative properties of the atmosphere. The consistency of the spectra over larger geographic areas and longer time periods must also be determined to ascertain their usefulness to investigations of climate variability. The geographic regions examined in this study are illustrated in Figure 3. Tropical boxes are limited to ocean only and extend from 5N to 5S. The Western Pacific (WP) and Eastern Pacific (EP) regions are each 60 degrees of longitude wide, while the Atlantic (AT) and Indian Ocean (IN) regions each cover 40 degrees of longitude. The African region over the Sahara Desert (AF) extends from 20N to 30N and 10W to 30E and generally excludes the Sahel to remove the surface inhomogeneities introduced by vegetation. The North Pacific (NP) and North Atlantic (NA) areas cover 40N to 50N and are respectively 80 degrees and 40 degrees wide in longitude.

3.1. Cloud Clearing Techniques

To facilitate the analysis of clear sky radiances only, a method of distinguishing clear spectra from those containing significant cloudiness is required. Three cloud clearing techniques have been examined. The most straightforward is the threshold approach, in which spectra are separated based on the radiance or brightness temperature at a selected wavenumber value or the integrated quantity over a frequency channel. Over the ocean, clear sky brightness temperatures at frequencies of high transparency are typically within a few degrees of the sea surface temperature. The difference is primarily a consequence of tropospheric water vapor absorption, but thin cloud or aerosol may contribute as well. For equatorial ocean regions where water vapor variability is low, a brightness temperature distribution can be used to select an appropriate threshold when the surface temperature is not known. Over land this technique is not as effective because land temperatures and

emissivities are typically not sufficiently uniform and water vapor absorption is generally more variable.

A second cloud clearing approach takes advantage of the spatial variability of radiance over an area. This spatial coherence method was developed to identify more accurately partially cloud-filled fields of view [Coakley and Bretherton, 1982] and has been studied in the context of the IRIS data. Radiance spectra have been examined for a single wavenumber channel and compared to neighboring spectra as ratios and differences to determine the presence of cloud induced opacity. In general, adjacent spectra were found to be too highly correlated to show any usable quantitative criteria for cloud determination [B. Haskins, private communication, 1994]. A third technique uses spectral information from several frequencies or channels and can also be used to distinguish clear spectra from cloud contaminated spectra and water clouds from ice clouds [Ackerman, et al., 1990]. Since the requirement for this study is to isolate the clearest spectra and not to determine cloud fraction, a carefully chosen threshold provides an adequate level of distinction. However, the problem of thin cirrus contamination from partially cloudy fields of view remains. It is assumed that all spectra that exceed the threshold are predominantly clear, and the results should be viewed from the perspective that the selected spectra have been interpreted as clear.

The histograms in Plate 1 show the seasonal distributions of brightness temperature at 1127.7 cm^{-1} for all spectra observed within the four tropical ocean regions between April, 1970 and January, 1971. The selection of 1127.7 cm^{-1} as the spectral basis for the distribution was primarily due to the high atmospheric transparency in this region. Also, the highest brightness temperature for the majority of clear spectra occurs at this wavenumber value and is therefore closest to the surface temperature, though it is still diminished by water vapor attenuation. In Plate 1 and all subsequent plots, the spring season is indicated by 'XAM' where the 'X' signifies the absence of March spectra from the dataset, the summer and fall seasons are 'JJA' and 'SON', and the winter season 'DJX'

excludes February. Each distribution is plotted as a percentage of the total number of spectra in that season, with a box width of 1 K. The large peaks at the warm end of each histogram represent the clearest spectra, while the remaining colder boxes correspond to various cloudy spectra.

The seasonal distributions shown in Plate 1 display variations that are consistent with the observed climatological patterns for each region. The prominent peaks from 291-300 K in the WP distributions (Plate 1a) include about 70% (found by summing across the warmest ten boxes) of the total spectra and are a combination of the roughly 45% frequency of clear sky [Rossow, 1993] and the nearly 30% frequency of thin cirrus [Prabhakara, et al., 1993] in the Western Pacific. In the EP region (Plate 1b), the number of spectra with peak brightness temperatures at or below 283 K is much less than the Western Pacific, while the number of spectra with temperatures between 284 K and 292 K is distinctly higher. This is indicative of fewer cold high clouds due to the diminished convection in the Eastern Pacific and more warm low or mid-level clouds that radiate closer to the surface temperature. The exception is the EP spring distribution which is similar to the Western Pacific pattern. In addition, the summer, fall and winter distribution peaks are lower by several degrees relative to the Western Pacific. The AT region, shown in Plate 1c, is similar to the Eastern Pacific except in spring, though more cold high clouds are present. The IN region (Plate 1d) displays the greater cloudiness associated with its proximity to the warm pool convection and the Indian monsoon.

Plate 2 illustrates the seasonal distributions for the remaining regions. Spectra from the desert area have been separated into nighttime (Plate 2a) and daytime (Plate 2b) distributions, and due to the Nimbus 4 orbit the spectra are all within a few hours of midnight or noon. For this region the distributions are based on the brightness temperature at 831.5 cm^{-1} to avoid the silicon dioxide absorption in the 1050 to 1250 cm^{-1} band [Salisbury and D'Aria, 1992]. The difference of roughly 25 K between Plates 2a and 2b is primarily a result of the large diurnal variation of surface temperature over the desert. In

addition, the seasonal variation of brightness temperature is also apparent and is approximately 18 K between the summer and winter. Brightness temperature distributions at 1127.7 cm^{-1} from the North Pacific (Plate 2c) and North Atlantic (Plate 2d) generally reflect the higher frequency of cloud cover in these areas with broader and smaller distribution peaks, while also showing greater seasonal variability than the tropical areas.

Selection of the temperature threshold for clear-sky definition is dependent on both geographic region and radiance variability in the longwave spectral window. Means and standard deviations of spectral brightness temperature were examined for groups of spectra as a function of threshold. Within the spectral window, it was found that selections of clear sky spectra reflect the relatively low variability of background sea surface emissions (Figure 4), and that the inclusion of cloudy spectra substantially increases the variability. Thresholds were selected which resulted in the largest group of spectra that maintained a low standard deviation. For all tropical ocean regions (Plate 1), the threshold was defined as the brightness temperature two degrees colder than the distribution peak. Although this may exclude a small number of clear cases, this criteria was chosen to isolate the warmest spectra and to reduce the number of spectra with very thin cirrus in the clear category. Over the Sahara Desert (Plates 2a and 2b) spectra are mostly clear, and a threshold 5-7 K below the peak was selected for both day and night spectra. Over the northern oceans (Plates 2c and 2d), the spectra with the warmest brightness temperatures represent either clear sky or warm low clouds. Spectral brightness temperature standard deviations were again examined, and the seasonally dependent thresholds were chosen several degrees warmer than the distribution peaks so that only the higher end of the distribution is assumed to be cloud free.

For each region and season, Table 1 lists the total number of IRIS radiance spectra, the number classified as clear, and the brightness temperature thresholds used to separate clear spectra from the total relative to the brightness temperature distributions in Plates 1 and 2. Geographic regions are identified as in Figure 3, except for 'AFN' and 'AFD'

which refer to nighttime and daytime spectra over the Sahara Desert respectively. Also included for comparison are the mean sea surface temperatures averaged over the same regions and seasons from April, 1970 through January, 1971. The SST dataset applied to this study is the filtered and gridded COADS (Comprehensive Ocean Atmosphere Data Set) monthly climatology of Reynolds, [1988]. Of particular interest is the Eastern Pacific spring mean SST of 299.9 K which is 2.5 - 3.2 K warmer than the other seasons in this region and is closer to the Western Pacific mean SSTs. The similarity of the Eastern Pacific spring distribution to those in the Western pacific (Plates 1a and 1b) may be a response to this similarity in mean ocean temperature. In general, the spring and winter seasons are underrepresented by a factor of two to three relative to summer and fall due to insufficient data. Clear spectra number from nearly 200 to over 1200 in most cases with the exception of the tropical Atlantic, North Atlantic, and nighttime Sahara regions during winter. The results for these cases should be interpreted cautiously given the smaller sample, the size of the regions, and the temporal extent being considered.

3.2. Seasonal Mean Brightness Temperature Spectra

The Western Pacific clear sky, seasonal mean brightness temperature spectra over the full 400-1600 cm^{-1} spectral range are shown in Figure 4a, and their standard deviations (σ_{bt}) are shown in Figure 4b. On this scale, the overall stability of the four curves, which represent 3500 spectra taken over a ten-month period, is remarkable, and this reinforces the reliability and quality of the dataset. Although the means are not weighted spatially or temporally, they generally extend across each region uniformly within the orbital restrictions of the satellite. Of particular note are the very low standard deviations in the 580-750 cm^{-1} CO_2 band (less than 1 K from 620-720 cm^{-1}), the 980-1080 cm^{-1} O_3 band, and across the window region. The 1-2 K σ_{bt} in the 800-1200 cm^{-1} window is consistent with the roughly 1 K standard deviation of tropical ocean temperatures over annual mean conditions including all modes of variability of duration less than a year [Peixoto and Oort, 1992]. The higher 4-5 K σ_{bt} in the water rotation band, 400-580 cm^{-1}, and the slightly

higher standard deviation from 750-820 cm^{-1} reflect the variability of tropical water vapor. Across this spectral region σ_{bt} would be continuous in the absence of CO_2. Standard deviation increases between 1200-1600 cm^{-1} are primarily due to the variability of upper tropospheric water vapor, the low radiances above 1400 cm^{-1} (see Figure 2a), and instrument noise above 1500 cm^{-1}. The spring season displays the lowest variability of water vapor as evidenced by the σ_{bt} from 400-580 cm^{-1} and from 1260-1450 cm^{-1}. Also note that the centers of the H_2O absorption lines, especially from 1150-1600 cm^{-1}, show greater variation than the regions between the lines. However, the primary absorption band of the uniformly mixed gas methane (centered at 1304 cm^{-1}) has a relatively low σ_{bt} for all seasons.

The standard deviation curves in Figure 4b have a shape that is closely related to the influence of atmospheric and surface variability on the outgoing spectral radiance. LBLRTM calculations of the effect on the outgoing spectral brightness temperature of individually varying the surface temperature, tropospheric temperature, and water column amount in a tropical atmosphere are shown in Figure 5. The two curves in Figure 5a represent the contribution of surface temperature increases of 1 K (light line) and 2 K (dark line) to the brightness temperature at the top of the atmosphere. Figure 5b shows the effect of increasing only the tropospheric temperature by 1 K (light line) and 2 K (dark line) at every level up through the tropopause. The two curves in Figure 5c represent the effect of increases in total water column amount of 10% (light line) and 20% (dark line). Decreases in these parameters would have effects that are symmetric and of opposite sign. Surface temperature variations are only apparent through the atmospheric infrared window from 710-1300 cm^{-1} and are most noticeable in the 1080-1200 cm^{-1} region between the strong water absorption lines. Tropospheric temperature changes are largest in the methane band near 1304 cm^{-1} and in the wings of the strongest CO_2 absorption where radiation emanates from near the tropopause, and at high and low wavenumber values. Water vapor changes (whether positive or negative) are most apparent in the strongly absorbing regions below

570 cm^{-1} and above 1300 cm^{-1}, and are least noticeable where absorption is dominated by CO_2 near 667 cm^{-1}, O_3 near 1040 cm^{-1}, and methane.

An expanded view of Figure 4 emphasizing the 800-1200 cm^{-1} window region is shown in Figure 6a and 6b. At the wavenumber values which display the warmest temperatures due to high atmospheric transmittance (e.g. 1128 cm^{-1}), the mean brightness temperature spectra for the four seasons are ordered from warmest to coldest identically to the observed seasonal mean SST (see Table 1) and are about 5 K lower than the mean SST. Although the spectral differences among the four curves appear to be small, they are significant and will be discussed in more detail in section 3.3. The curvature in σ_{bt} is a response of the intraseasonal spectral variability in outgoing brightness temperature to atmospheric and surface variations among hundreds of spectra similar to the calculated changes shown in Figure 5. Both positive and negative departures of atmospheric temperature and water vapor amount from the seasonal mean would cause a higher standard deviation at either end of the 800-1200 cm^{-1} range relative to the central frequency. Since surface temperature variations contribute a curvature in the opposite sense and offset the atmospheric effects, it is proposed that atmospheric variability is substantial enough in the Western Pacific to counteract the 1 K sea surface temperature variability based on the curvature of σ_{bt} in Figure 6b. Also, the highest standard deviations occur in the center of the strongest absorption lines, indicating their sensitivity to atmospheric water vapor which is more variable over the tropical oceans than the background sea surface temperature emission. It can be seen from Figure 5a that surface temperature variations would preferentially increase σ_{bt} between the water absorption lines. Thus, both the upward curvature and the magnitude of the spectral features in σ_{bt} indicate the presence of discernible atmospheric variability.

The Eastern Pacific clear sky mean brightness temperature and σ_{bt} for the four seasons are shown in Figures 6c and 6d. Once again, the seasonal mean spectra are ordered from warmest to coldest in close relation to the observed mean SST, with the

1127.7 cm^{-1} brightness temperatures roughly 3-4 K lower than the mean SST. The primary difference among the seasonal plots is a downward shift in brightness temperature relative to the Western Pacific due to the colder ocean temperatures. As in the Western Pacific, the curves are most similar in the centers of the strongest absorption lines, where the surface differences have a smaller contribution. The curvature of σ_{bt} during spring is similar to that seen in the Western Pacific, though less pronounced. This is consistent with the SST and distribution similarities between the EP spring and the WP seasons discussed earlier. The summer, fall, and winter standard deviations are considerably flatter, indicating either less atmospheric variability (reducing the curvature) or more surface variability (offsetting the curvature due to the atmosphere) relative to the Western Pacific.

Figures 7a and 7b show the clear sky seasonal mean brightness temperatures and standard deviations in the window region for the Atlantic region. The means are roughly 3K colder than the Western Pacific and similar to the means from the Eastern Pacific, though with generally smaller seasonal differences. The standard deviations differ more from season to season than in the Pacific though most display the upward curvature at either end of the spectral range indicative of atmospheric variability. The plots for the Indian Ocean region are shown in Figures 7c and 7d. Of note are the larger spectral features in the seasonal means associated with the water vapor absorption lines. The higher σ_{bt} in summer over the Indian Ocean and its reduced spectral features indicate more surface variability than the other seasons. Among the four tropical ocean regions the seasonal variations are clear signals in the outgoing spectral radiance associated with differences in atmospheric water vapor, temperature profiles, and surface temperature. The interseasonal variability is explored further in section 4.

Immediately apparent in the plots of seasonal mean brightness temperature over the Sahara Desert in Figure 8 is the absorption due to desert aerosols, primarily quartz sand (silicon dioxide). This reststrahlen absorption extends from 1050 to 1250 cm^{-1} [Salisbury and D'Aria, 1992] and is present in all seasons for both night (Figure 8a) and day (Figure

8c) spectra. Note the scales for both brightness temperature and standard deviation in Figure 8 are increased by a factor of two from Figures 6 and 7. The apparent seasonal cycle is consistent with the roughly 18 K observed annual cycle of surface air temperature over the Sahara Desert (National Climatic Data Center, 1994). The slope of brightness temperature in the 800 to 1000 cm^{-1} band is slightly negative due to the emissive properties of the land surface, in contrast with the water induced positive slopes seen over the oceans. The diminished spectral features of the nighttime means relative to those at mid-day demonstrate the effect of the more isothermal, nighttime temperature profiles on the longwave emissions compared to the large lapse rate conditions during the heat of the day. Also, the σ_{bt} for night and day (Figures 8b and 8d) are higher overall than the tropical ocean area, show more seasonal variation, and are slightly higher in the silicon absorption band, especially for the spring and summer seasons. It is also interesting to note that the standard deviations are highest for the frequencies between the water vapor lines, rather than at the water vapor lines as was typical of the tropical ocean spectra. This slightly higher variability in the emitted brightness temperature at the silicon absorption frequencies could result from either inhomogeneities in the surface over the examined region or variations in the distribution of airborne silicate material.

Clear sky seasonal mean brightness temperature spectra for the Northern Pacific region are shown in Figure 9a along with their standard deviation in Figure 9b. Here the scale for σ_{bt} is twice that for Figures 6 and 7. Not surprisingly, the summer and fall seasons are warmer than winter and spring. Also noteworthy are the flatter (more positive) slopes of brightness temperature across the 800-1000 cm^{-1} region relative to the tropical mean spectra as well as the smaller spectral features overall. These are primarily a result of the lower water vapor content and shallower lapse rates of the mid-latitude atmosphere. The higher standard deviation in the 1000-1070 cm^{-1} ozone band in winter and spring is a result of the greater intraseasonal ozone variability in the middle and high latitudes during the cold seasons [Report of the International Ozone Trends Panel, 1988]. Ozone

production occurs predominantly in the tropical stratosphere and drops substantially during the colder months at higher latitudes due to the decrease in solar radiation. Thus, where ozone is not being replenished the ozone column and its radiative effects are subject to greater variability due to transport within the atmospheric general circulation. The drop in standard deviation at the 1043 cm^{-1} center of the ozone band corresponds to a decrease in ozone absorption where the surface contribution is significant. The background σ_{bt} across the window region of about 2.4 K is consistent with the roughly 3 K day-to-day standard deviation of ocean temperatures in the 40-50N latitude band for annual mean conditions [Peixoto and Oort, 1992]. In addition, the σ_{bt} curves generally show a slight downward curvature and higher values between the water absorption lines, which indicates that the SST variations slightly dominate the atmospheric variability in this region. Similar comments can be made for the corresponding plots from the North Atlantic region in Figures 9c and 9d.

3.3. Seasonal Spectral Radiance Differences

In order to illustrate the relationship between the spectral features discussed in the previous section and the seasonal and regional climate variations during this annual cycle and to assess the effectiveness of that relationship as a diagnostic of climate change, we examine differences between the seasonal mean spectra and the full ten-month mean spectra for the six ocean regions. For present purposes, we refer to the April, 1970 to January, 1971 ten-month mean as an approximation of the annual mean. The differences are analyzed in units of radiance rather than brightness temperature, since radiance is the observed parameter and the discussion will lead directly to the atmospheric retrieval section that follows.

Annual mean radiance spectra were produced for each ocean region from the seasonal means presented in Figures 6, 7, and 9. Figure 10a shows the clear sky spectral radiance differences for the Western Pacific region with the annual mean ('ANN') subtracted from each seasonal mean. Several striking features are apparent. Once again,

the very low variation in the CO_2 band is observed for all seasons except winter. The small variations that are present from 630-700 cm^{-1} are likely a result of small changes in the generally stable tropical tropopause and lower stratospheric temperatures. The winter 1970-71 departure from the annual mean radiance is an indication of the decrease in lower stratospheric tropical temperature which peaked in early January, 1971 as observed by the Selective Chopper Radiometer aboard Nimbus 4 [Barnett, 1974]. This tropical cooling was accompanied by a dramatic stratospheric warming at the poles during this period. The sudden change in lower stratospheric tropical temperature is further evidenced by the increase in brightness temperature standard deviation in the 630-700 cm^{-1} band during the 1970-71 winter season (see Figure 4). At all other frequencies, the spring season displays the largest spectral deviations. The summer season shows a uniformly positive shift from the annual mean except in the ozone band (1000-1080 cm^{-1}) with little spectral variation associated with the water vapor lines. In the ozone band, variations are smaller since the outgoing radiance is emitted primarily from the upper atmosphere and tropospheric changes have less of an impact. Fall and winter each show spectral variation from the annual mean with winter displaying a shift in the window region of 1.3 (mW m^{-2} sr^{-1})/cm^{-1} in the opposite sense of the summer shift.

Figure 10b contains the seasonal minus annual mean radiance differences for the Eastern Pacific region. Here, the spring season departure from the annual mean is spectrally very similar to the spring difference in the Western Pacific, but it includes a larger positive departure in the window region of as much as 2 (mW m^{-2} sr^{-1})/cm^{-1}. This suggests a warmer mean sea surface temperature in this season based on the calculated brightness temperature changes in Figure 5a, and this is confirmed by the observed SSTs in Table 1. If the curves in Figure 5 are plotted in radiance, the magnitude of the differences in the 1250-1600 cm^{-1} region would be significantly reduced relative to the 450-1000 cm^{-1} region due to the shape of the Planck function. The fall season shows a 1.5 (mW m^{-2} sr^{-1})/cm^{-1} negative departure from the annual mean radiance in the window

region, which is consistent with the observed low SST. These spring and fall differences are reversed in the water vapor rotation band from 400-600 cm^{-1}, where the spring season has a large negative departure that is balanced by the smaller positive differences in summer and fall. This suggests a larger mean water vapor content in spring and lower water vapor amounts in the fall relative to the annual mean, though the seasonal mean variations are likely due to a complex combination of atmospheric and surface changes. Finally, it is instructive to think of the differences in the CO_2 and O_3 bands as interruptions in the curves, which would be continuous if carbon dioxide and ozone were not present to obscure the effects of water and temperature in the troposphere. This will be discussed in more detail in the following section on atmospheric parameter retrieval.

The clear sky spectral radiance differences between the seasonal and annual mean spectra are shown for the tropical Atlantic Ocean in Figure 11a and the tropical Indian Ocean in Figure 11b. In the Atlantic, the spring season once again displays the spectral features indicative of a higher water vapor content and warmer SST, though here the water departure somewhat outweighs the surface temperature change. In the 400-600 cm^{-1} band, the seasonal patterns are very similar to those seen in the Pacific. However, for the Indian Ocean, the most notable departure from the other tropical regions occurs in this spectral region. The spring season over the Indian Ocean displays a slight positive difference, while the largest deficiency in outgoing radiance relative to the annual mean, and thus the greatest water vapor increase, has shifted to summer. This is consistent with the timing of the summer Indian monsoon, though precipitable water increases over the equatorial Indian Ocean are typically smaller than those over the Indian continent during an active monsoon. The magnitude of the spectral features in this band are larger than for any other tropical region, however, and they also imply a more complex explanation for the radiance differences involving several atmospheric parameters. Finally, note that in all four regions shown in Figures 10 and 11, the seasonal radiance differences from the annual mean in the CO_2 band are nearly identical. This illustrates both the stability of the IRIS measurements

(Figures 10 and 11 were derived from over 9000 clear sky spectra) and the zonal symmetry of stratospheric temperatures in the tropics during this annual cycle, including the colder winter period.

The corresponding radiance differences for the North Pacific and North Atlantic regions are shown in Figure 12a and 12b. The expected seasonal effects of the warmer, wetter summer and fall, and the colder, drier winter and spring are present across the window and water rotation bands. Higher in the atmosphere, as seen in the 630-700 cm^{-1} radiance differences, the spring and fall seasons reverse sign. This is a response of the stratospheric temperature to both the mid-June peak in the incident solar radiation and the spring peak in the total ozone amount observed in the extratropical latitudes of the Northern Hemisphere [Ozone Trends Panel, 1988].

4. Spectral Radiance Retrievals

It was shown in the previous section that the difference between seasonal and annual mean outgoing IRIS radiance can be qualitatively associated with variations in atmospheric parameters. A linear retrieval algorithm has been used to quantify the significant seasonal variations in surface and air temperature, water column amount, water and temperature lapse rates, and ozone amount from the clear sky, tropical, mean radiance differences in Figures 10 and 11. The low standard deviations of the mean radiances in the 600-1200 cm^{-1} region support the retrieval of atmospheric parameters with this frequency range on the assumption that the individual spectra are similar to the mean spectrum. Although it is generally inappropriate to perform retrievals on averaged spectral radiances to obtain an average atmospheric state, in the case of low atmospheric variability, such as the tropics, it is appropriate to infer the difference in atmospheric state from the difference in mean spectral radiances.

4.1. Retrieval Model and Implementation

The retrieval procedure has been applied over the 430-1200 cm^{-1} spectral range excluding the band of strong CO_2 absorption from 610-730 cm^{-1}. The primary ozone

absorption band is included in the retrieval because of its overlap with tropospheric water vapor that occurs in this region. A portion of the water vapor pure rotation band from 430-610 cm^{-1} is also included because of the important information it contains about the middle and upper tropospheric water vapor. Spectral radiance standard deviations within this band are two to three times higher than in the window region (see Figure 4), but they are considered to be sufficiently small to warrant inclusion, since the radiance in this region contributes significant information to the retrieval. For a single tropospheric layer from the surface to 17 km, the algorithm obtains the variations in several atmospheric variables which correspond to the seasonal minus annual mean radiance difference for each region.

The retrieval algorithm utilizes a physical least squares method to derive atmospheric state parameters from radiance measurements and has been described and applied in the context of tropospheric ozone retrievals [Clough, et al., 1995]. Derivatives for each parameter are determined by perturbing the initial atmospheric state and performing a forward calculation using a line-by-line radiative transfer model (LBLRTM). For this study, the standard tropical profile is used as the initial, or reference, state since it provides an appropriate first guess to the equatorial mean radiance spectra being analyzed. The least squares algorithm is then applied to minimize the radiance residual between the seasonal and annual mean spectra for the selected parameters. Rather than performing retrievals from observed radiance spectra, this approach requires that the seasonal minus annual mean radiance difference be the only measured quantity to enter the algorithm. Sea surface temperature, layer temperature, water column amount, and temperature and water lapse rates were retrieved for the single tropospheric layer. Lapse rate changes are accomplished for the single layer case by perturbing the upper level value while keeping the surface fixed and maintaining a linear variation in the layer. Ozone column amounts are retrieved for a single layer from 0 to 50 km. In most cases this procedure reduced the radiance difference such that the noise variance of the resulting residual approaches that of the observed data and is consistent with the variance of the atmospheric state. Finally, the retrieved variations

in the atmospheric parameters represent the change in atmospheric conditions which would be necessary to account for the observed differences between the seasonal and annual mean radiance spectra over the tropics.

4.2. Tropical Pacific Retrievals

Retrieval effectiveness can be demonstrated by examining the extent to which the radiance residuals are minimized. For the seasonal mean spectral radiance differences shown in Figure 10, the resulting differences after the parameter retrieval are shown in Figure 13a for the Western Pacific and in Figure 13b for the Eastern Pacific. In each case the residual radiance difference has been reduced by an order of magnitude at all wavenumbers above 730 cm^{-1}. The curves are essentially unchanged in the CO_2 band since this region was excluded from the retrieval. In the water absorption band at low wavenumbers appreciable differences remain, though they are generally reduced to less than 0.5 $(mW\ m^{-2}\ sr^{-1})/cm^{-1}$ except at the centers of the strongest water absorption lines.

The retrieved seasonal changes in atmospheric state parameters for the Western and Eastern Pacific cases presented in Figures 10 and 13 are listed in Table 2. Changes in ozone column amount, water vapor column amount, ΔW(column), and water lapse rate, $\Delta W/\Delta Z$, are given in percent. The sea surface temperature, ΔTs, tropospheric layer temperature, ΔT(layer), and tropospheric temperature lapse rate, $\Delta T/\Delta Z$, variations are also indicated. Also included in the table are the observed seasonal minus annual mean SST differences, ΔTs(obs), averaged over the same regions and seasons [Reynolds, 1988]. Finally, the variance ratio (VR) of each retrieval is shown. This ratio is defined as the actual spectral variance of the result to the predicted variance based on the instrument measurement error. A low value indicates a better fit to the seasonal radiance differences from the mean. The values are less than unity because the effects of spectral averaging to obtain the seasonal means have not been taken into account in the theoretical variance.

The difference between the retrieved SST change and the observed seasonal SST change [ΔTs-ΔTs(obs)] is within 0.2-0.7 K for all cases in Table 2. For the Western and

Eastern Pacific, both the retrieved and observed SSTs decrease during the year relative to the ten-month mean. Ocean temperatures across the tropical Pacific became increasingly colder than normal throughout the ten-month IRIS observation period as a moderate Southern Oscillation cold event, or La Nina conditions, developed during the summer of 1970 and continued into early 1971 [Meehl, 1987]. Negative SST anomalies of up to 1 K were present especially in the eastern equatorial Pacific in late 1970 [Philander, 1985]. In addition, tropical radiosonde measurements indicate that tropospheric temperatures also decreased during 1970 in response to the colder ocean [Angell and Korshover, 1983].

In general, the climate in the tropics is dominated by the sea surface temperature, and the retrieved, seasonal, atmospheric parameter changes for clear sky conditions during 1970 follow this pattern. For the seasons with SSTs above the annual average (spring and summer in the Western Pacific and spring in the Eastern Pacific), the tropospheric temperature is retrieved with a positive change in the layer temperature and an increase in the lapse rate. Note that for the lapse rate parameters, a positive value corresponds to an increase in the lapse rate. The colder SSTs later in the year generally produce lower tropospheric temperatures and decreased lapse rates. In addition, the retrieval produces the expected increase in water column amount due to greater evaporation over the warm ocean early in the year and the decrease in atmospheric water vapor during the colder fall and winter across the tropical Pacific. It should be emphasized that these results are for mean clear sky conditions, and that the influence of cloud cover is involved only indirectly.

A comparison of the data in Table 2 with the seasonal mean radiance differences of Figure 10 illustrates the extent to which the interseasonal climate variations during 1970 are apparent in the spectral radiance. For example, during spring in the Western Pacific, the retrieved 9.1% increase in water vapor column accounts for the lower outgoing radiance below 600 cm^{-1}, which is consistent with the calculations in Figure 5. This effect is partly offset by an atmosphere that is warmer throughout the troposphere, as determined by combining the layer and lapse rate changes. In order to enhance their interpretation, the

seasonal variations in tropospheric water vapor and temperature in Table 2 are illustrated in Plate 3. The upper row of Plate 3 shows the percent change in the seasonal water vapor profiles relative to the annual mean for each tropical region. Seasonal changes in the temperature profiles are shown in the bottom row of Plate 3, and the retrieved SST changes are marked with triangles along the lower axes. Note that profile changes with positive slopes indicate decreased lapse rates relative to the annual mean. For spring in the Eastern Pacific the water column increase is only 4.3% due to the smaller change near the surface, but large increases in temperature lapse rate (0.13 K/km) and tropospheric temperature (1.53 K) result in a colder upper troposphere. The lowered water vapor lapse rates during spring in both Pacific regions are a result of increased moisture in the upper troposphere, which further contributes to decreasing the outgoing radiances by causing more water vapor emission at colder temperatures. Also, the large spectral features during spring at all frequencies outside the CO_2 band are due to a combination of the higher water column, the higher surface temperature, the greater temperature lapse rate (which magnifies the contrast between the emission temperatures near surface and higher in the atmosphere), and the lowered water vapor lapse rate. Finally, the higher surface temperatures of 1.0 K in the west and 1.6 K in the east push the overall radiance difference upward in spring between 750 and 1250 cm^{-1}, where the surface effects dominate as shown in Figure 5. Note that the water vapor column amount, the tropospheric temperature, and the lapse rates all interact to generate the radiance differences, especially at the lower wavenumber values outside the CO_2 region.

In summer over the Western Pacific, water changes are small and the warmer temperatures increase the outgoing radiance. The increased temperature and water lapse rates partially offset each other to limit the magnitude of the spectral features. In the Eastern Pacific summer, the temperature changes are small, and the higher water column and lapse rate act to raise the outgoing radiance from 400-600 cm^{-1} (Figure 10b) by increasing the water vapor closer the surface relative to the other seasons and increasing its

emission temperature. In fall over both Pacific regions, the large water column deficits and steeper water lapse rates increase the radiance at low wavenumbers, while the colder temperatures lower the radiance at higher wavenumbers. The decreases in temperature lapse rate during fall (Plate 3) magnify the spectral features relative to the annual mean, though in the opposite sense of the spring season changes. Finally, during winter over the Western Pacific the relatively small water changes combine with the colder temperatures to lower the outgoing radiance over the whole spectral range. In the Eastern Pacific winter, the small outgoing radiance difference above 750 cm^{-1} is due to a balance between the much lower water column and the colder surface and tropospheric temperatures.

4.3. Tropical Atlantic and Indian Ocean Retrievals

The retrieved changes in atmospheric parameters for the Atlantic and Indian Ocean spectral radiance differences presented in Figure 11 are listed in Table 3, and the seasonal profile changes are illustrated in Plate 3. Here, the retrieved SST changes are within 0.1-0.7 K of the observed values except for spring and summer in the Indian Ocean, which are within 1 K. In general, the discussion of the relationship between the retrieved interseasonal variability and the seasonal radiance differences for the Pacific applies to the Atlantic and Indian Ocean areas. Of particular interest from the Atlantic region are the consequences of the large surplus in water column amount of 16% and the decreased water lapse rate in spring which strongly lower the outgoing radiance and offset the +0.9 K departure in SST. In contrast, the water column excess over the Indian Ocean in spring is dramatically offset by a steeper water lapse rate and warmer temperatures to produce higher radiances. However, the water column excess and colder SST in summer decrease the outgoing radiance despite the warmer lower troposphere. Also, note that the retrieved changes in ozone column amount for each season in all four tropical regions are consistent with the spectral radiance differences after the shifts in atmospheric and sea surface temperature are considered. It should be noted that the radiance residuals after the retrieval

of the Atlantic and Indian Ocean parameters are consistent with the improvement shown in Figure 13 for the tropical Pacific regions.

The most dramatic feature of the tropical retrievals is the apparent signature of the summer Indian monsoon, which was stronger than normal during the summer of 1970 [Meehl, 1987]. The greater frequency of cloud cover and precipitation over the tropical Indian Ocean relative to the other tropical regions lowers the number of clear sky spectra to about 30% of the total (see Table 1). This is associated with both the monsoon to the north and the enhanced warm pool convection to the east and reduces the spatial and temporal coverage of the clear radiance spectra in each season. The monsoon dynamics more readily redistribute the available water vapor as evidenced by the extremes of horizontal water vapor divergence that occur in this area [Peixoto and Oort, 1992]. This produces the large retrieved seasonal variations in water column amount of 12-22% and in water lapse rate over the clear sky Indian Ocean seen in Table 3. The greatest seasonal water column decrease in this region of 34% occurs from summer to fall, and Plate 3 shows that the largest seasonal changes over the equatorial Indian ocean occur in the lower troposphere. In addition, the substantial decrease in temperature lapse rate from summer to fall in this region is a combined response of the tropospheric temperature profile to the longwave radiative cooling due to the diminished water column and the transport of latent heat generated by the strong indigenous convection. Finally, it should be emphasized that the linear changes in Plate 3 are not retrieved profiles but are clear indications of the relative interseasonal variability as obtained from the clear sky mean spectral radiances.

5. Summary and Conclusions

The IRIS longwave spectral radiance dataset provides unique information for examining the relationship between outgoing longwave radiation and atmospheric variations. The advantages of spectral radiance over integrated quantities include identifying the effects of individual greenhouse gases such as water vapor, carbon dioxide, ozone, and methane, as well as detecting complex temperature effects such as changes in

tropospheric lapse rate. IRIS radiances were validated against a line-by-line model and were shown to reproduce the infrared spectrum within a few (mW m^{-2} sr^{-1})/cm^{-1} for the tropical and mid-latitude clear sky cases examined once errors in atmospheric specification were identified.

Regional and seasonal means of brightness temperature over the equatorial and northern oceans are shown to be sufficiently consistent to examine interseasonal variations within the ten-month extent of the IRIS data after removal of erroneous spectra. Clear sky mean spectra show characteristic signatures such as the magnitude of spectral line features and the shape of the background radiance in the thermal window region which correspond to properties of the emitting surface and the absorbing and reemitting atmosphere. This relationship between spectral signatures and atmospheric parameters has been quantified for clear sky tropical ocean regions and shown to correspond to the observed conditions during the 1970 annual cycle. Specifically, regional and seasonal mean sea surface temperatures were retrieved to within 0.2-0.7 K of observed values despite the decreasing SSTs that existed, especially in the Pacific Ocean, during 1970. In addition, seasonal water column variations from the annual mean were shown to vary from 5-20% in the tropics depending on the region, generally in response to ocean temperature changes or the Indian monsoon.

Standard deviations of clear sky brightness temperature spectra were studied for both land and ocean areas. Across the 8-12 μm window region they were found to be 1-2 K for tropical oceans and 2-3 K for northern mid-latitude oceans, which are consistent with the observed SST variability. The remarkably low standard deviations of less than 1 K within the CO_2 band, which occur in all the tropical regions examined, demonstrate the stability of the IRIS data. Standard deviations of brightness temperature spectra over the mid-latitude oceans capture the greater variability of ozone amount due to diminished ozone production and increased transport during the cold seasons. In general, the shape of the spectral standard deviation is very effective at illustrating the relative variability between background surface emissions and those from the intervening atmosphere.

Spectral radiances contain important atmospheric information relevant to global climate change, and the demonstrated capability of identifying surface and atmospheric variations from spectral radiances supports their use as a diagnostic for longwave radiation codes such as those in 3-D general circulation models (GCMs). Ideally, GCMs should reproduce the spectral mean radiances within the limitation of their spectral resolution. Measured spectral radiances provide the flexibility to compare with output from any lower resolution radiation band model. In addition, a GCM which reproduces the seasonal and regional variances of outgoing longwave radiation would further enhance its validation. Comparison with observed quantities is imperative for comprehensive GCM validation, and longwave spectral radiances provide relevant and detailed information about the absorption and emission of greenhouse gases, the temperature structure of the troposphere and lower stratosphere, and radiative properties of the surface, in addition to the spectral cloud radiative properties not examined in this study. Furthermore, as GCM radiation codes become faster and higher spectral resolution becomes more feasible, these measurements will become even more essential.

The use of spectral radiance as a diagnostic for climate simulations clearly necessitates a longer measurement period than the ten months provided by IRIS. This single annual cycle of data illustrates the capability of identifying signatures of atmospheric variability in longwave spectral radiances, but it does not establish the impact of long term changes. Future instruments such as AIRS will begin to provide such data and continue to clarify the important connection between spectral radiance and climate variability.

Acknowledgments

The authors would like to thank R. Hanel and the National Space Science Data Center for providing the magnetic tapes containing the original IRIS data. Thanks to R. Haskins for his ideas and discussions during the course of the work and to R. M. Goody for his contributions during the conception of the project. This work was supported by the National Aeronautics and Space Administration under grant NASW-4752.

References

Ackerman, S. A., W. L. Smith, J. D. Spinhirne, and H. E. Revercomb, The 27-28 October 1986 FIRE IFO cirrus case study: spectral properties of cirrus clouds in the 8-12 μm window, Mon. Wea. Rev., 118, 2377-2388, 1990.

Anderson, G. P., S. A. Clough, F. X. Kneizys, J. H. Chetwynd, and E. P. Shettle, AFGL atmospheric constituent profiles (0-120 km), Rep. AFGL-TR-86-0110, Air Force Geophys. Lab., Hanscom Air Force Base, Bedford, MA, 43 pp., 1986.

Angell, J. K., and J. Korshover, Global temperature variations in the troposphere and stratosphere, 1958-1982, Mon. Wea. Rev., 111, 901-921, 1983.

Barnett, J. J., The mean meridional temperature behavior of the stratosphere from November 1970 to November 1971 derived from measurements by the Selective Chopper Radiometer on Nimbus 4, Q. J. R. Meteorol. Soc., 100, 505-530, 1974.

Bell, R. J., Introductory Fourier Transform Spectroscopy. 329 pp., Academic Press, Orlando, FL, 1972.

Clough, S. A., and M. J. Iacono, Line-by-line calculation of atmospheric fluxes and cooling rates II: application to carbon dioxide, ozone, methane, nitrous oxide, and the halocarbons, J. Geophys. Res., 100, 16519-16536, 1995.

Clough, S. A., C. P. Rinsland, and P. D. Brown, Retrieval of tropospheric ozone from simulations of nadir spectral radiances as observed from space, J. Geophys. Res., 100, 16579-16594, 1995.

Coakley, J. A., and F. P. Bretherton, Cloud cover from high-resolution scanner data: detecting and allowing for partially filled fields of view, J. Geophys. Res., 87, 4917-4932, 1982.

Elliott, W. P., and D. J. Gaffen, On the utility of radiosonde humidity archives for climate studies, Bull. Am. Meteorol. Soc., 72, 1507-1520, 1991.

Hanel, R. A., B. Schlachman, D. Rogers, and D. Vanous, The Nimbus 4 Michelson interferometer, Appl. Opt., 10, 1376-1382, 1971.

Hanel, R. A., B. J. Conrath, V. G. Kunde, C. Prabhakara, I. Revah, V. V. Salomonson, and G. Wolford, The NIMBUS 4 infrared spectroscopy experiment 1: calibrated thermal emission spectra, J. Geophys. Res., 77, 2629-2641, 1972.

Harrison, E. F., P. Minnis, B. R. Barkstrom, and G. G. Gibson, Radiation budget at the top of the atmosphere, in Atlas of Satellite Observations Related to Global Change, edited by R. J. Gurney, J. L. Foster, and C. L. Parkinson, pp. 19-38, Cambridge Univ. Press, New York, 1993.

Kunde, V. G., B. J. Conrath, R. A. Hanel, W. C. Maguire, C. Prabhakara, and V. V. Salomonson, The Nimbus 4 infrared spectroscopy experiment 2: comparison of observed and theoretical radiances from 425-1450 cm^{-1}, J. Geophys. Res., 79, 777-784, 1974.

Masuda, K., T. Takashima, Y. Takayama, Emissivity of pure and sea waters for the model sea surface in the infrared window regions, Rem. Sens. Environ., 24, 313-329, 1988.

Meehl, G. A., The annual cycle and interannual variability in the tropical Pacific and Indian Ocean regions, Mon. Wea. Rev., 115, 27-50, 1987.

National Climatic Data Center, Monthly Climatic Data for the World, 47, Nos. 1-12, NOAA, NCDC, Asheville, NC, 1994.

Peixoto, J. P, and A. H. Oort, Physics of Climate, 520 pp., Amer. Inst. Physics, New York, 1992.

Philander, S. G. H., El Nino and La Nina, J. Atmos. Sci., 42, 2652-2662, 1985.

Prabhakara, C., G. Dalu, V. G. Kunde, Estimation of sea surface temperature from remote sensing in the 11 to 13 μm window region, J. Geophys. Res., 19, 5039-5044, 1974.

Prabhakara, C., D. P. Kratz, J.-M. Yoo, G. Dalu, and A. Vernekar, Optically thin cirrus clouds: radiative impact on the warm pool, J. Quant. Spectrosc. Radiat. Transfer, 49, 467-483, 1993.

Report of the International Ozone Trends Panel, World Meteorological Organization, Geneva, Switzerland, Report #18, 1988.

Reynolds, R. W., A real-time global sea surface temperature analysis, J. of Climate, 1, 75-86, 1988.

Rossow, W., Clouds, in Atlas of Satellite Observations Related to Global Change, edited by R. J. Gurney, J. L. Foster, and C. L. Parkinson, pp. 141-163, Cambridge Univ. Press, New York, 1993.

Salisbury, J. W., and D. M. D'Aria, Emissivity of terrestrial materials in the 8-14 μm atmospheric window, Remote Sens. Environ., 42, 83-106, 1992.

Sinha, A., and J. E. Harries, Water vapor and greenhouse trapping: the role of far infrared absorption, Geophys. Res. Lett., 22, 2147-2150, 1995.

Smith, W. L., R. O. Knuteson, H. E. Revercomb, W. Feltz, H. B. Howell, W. P. Menzel, N. Nalli, O. Brown, J. Brown, P. Minnett, and W. McKeown, Observations of the infrared radiative properties of the ocean - implications for the measurement of sea surface temperature via satellite remote sensing, Bull. Am. Meteorol. Soc., in press, 1995.

Spankuch, D., and W. Dohler, Radiative profiles of cirrus clouds in the middle IR derived from Fourier spectrometer measurements from space, Z. Meteor., 6, 314-324, 1985.

Strong, A. E., and E. P. McClain, Improved ocean surface temperatures from space - comparisons with drifting buoys, Bull. Am. Meteorol. Soc., 65, 138-142, 1984.

Susskind, J., Water vapor and temperature, in Atlas of Satellite Observations Related to Global Change, edited by R. J. Gurney, J. L. Foster, and C. L. Parkinson, pp. 89-128, Cambridge Univ. Press, New York, 1993.

M. J. Iacono, and S. A. Clough, Atmospheric and Environmental Research, Inc., 840 Memorial Drive, Cambridge, MA 02139. (e-mail: mike@aer.com)

Figure Captions

Figure 1: Profiles of (a) temperature, and (b) water vapor for Guam on April 27, 1970. Temperatures below 25 km and water vapor below 10 km are from a 0000 UT radiosonde measurement, and data above these levels are from the standard tropical atmosphere.

Figure 2: Longwave radiance spectra from (a) an LBLRTM calculation based on the profiles in Figure 1 and an IRIS observation near Guam at 0202 UT on April 27, 1970, (b) IRIS-LBLRTM radiance difference of the spectra in (a) for the field of view corrected calculation, (c) IRIS-LBLRTM radiance difference near Guam at 1200 UT 12 July, 1970, and (d) IRIS-LBLRTM radiance difference near Guam at 0000 UT 13 July, 1970.

Figure 3: Geographic regions examined in this study. 'WP' refers to Western Pacific, 'EP' to Eastern Pacific, 'AT' to Atlantic Ocean, 'IN' to Indian Ocean, 'AF' to Sahara Desert, 'NP' to North Pacific, and 'NA' to North Atlantic.

Figure 4: Western Pacific 1970-71 seasonal brightness temperature (a) mean spectra and (b) standard deviations for the full IRIS spectral range.

Figure 5: LBLRTM calculations of the effect on outgoing spectral brightness temperature for (a) surface temperature increases of 1 K (light) and 2 K (dark), (b) tropospheric temperature increases of 1 K (light) and 2 K (dark), and (c) water vapor column increases of 10% (light) and 20% (dark).

Figure 6: Western Pacific 1970-71 seasonal brightness temperature (a) mean spectra and (b) standard deviations, σ_{bt}, in the infrared window region; and Eastern Pacific seasonal brightness temperature (c) means and (d) standard deviations.

Figure 7: Equatorial Atlantic 1970-71 seasonal brightness temperature (a) mean spectra and (b) standard deviations, σ_{bt}, in the infrared window region; and equatorial Indian Ocean seasonal brightness temperature (c) means and (d) standard deviations.

Figure 8: Sahara Desert 1970-71 nighttime seasonal mean brightness temperature (a) mean spectra and (b) standard deviations, σ_{bt}, in the infrared window region; and Sahara Desert daytime seasonal brightness temperature (c) means and (d) standard deviations.

Figure 9: North Pacific 1970-71 seasonal brightness temperature (a) mean spectra and (b) standard deviations, σ_{bt}, in the infrared window region; and North Atlantic seasonal brightness temperature (c) means and (d) standard deviations.

Figure 10: Seasonal minus annual mean IRIS radiance differences for the tropical (a) Western Pacific, and (b) Eastern Pacific from 1970-71.

Figure 11: Seasonal minus annual mean IRIS radiance differences for the tropical (a) Atlantic Ocean, and (b) Indian Ocean for 1970-71.

Figure 12: Seasonal minus annual mean IRIS radiance differences for the (a) North Pacific and (b) North Atlantic for 1970-71.

Figure 13: Retrieved seasonal minus annual mean radiance differences for the (a) Western Pacific and (b) Eastern Pacific after the six-parameter tropospheric retrieval which excluded the 610-730 cm^{-1} carbon dioxide region. Initial spectral residuals are shown in Figure 10.

Plate Captions

Plate 1: Seasonal distributions of 1127.7 cm^{-1} IRIS brightness temperature for 1970-71 conditions over the (a) Western Pacific, (b) Eastern Pacific, (c) Atlantic Ocean, and (d) Indian Ocean regions. The number of spectra at each temperature is plotted as a percentage of the total spectra for each season at intervals of 1 K.

Plate 2: Seasonal distributions of 831.5 cm^{-1} IRIS brightness temperature for 1970-71 conditions over the (a) nighttime Sahara Desert and (b) daytime Sahara Desert, and seasonal distributions of 1127.7 cm^{-1} brightness temperature over the (c) North Pacific, and (d) North Atlantic regions. The number of spectra at each temperature is plotted as a percentage of the total spectra for each season at intervals of 1 K.

Plate 3: Seasonal profile variations from the annual mean based on the retrieved parameter changes in Tables 2 and 3. Water vapor profile changes (upper row) for the Western Pacific, Eastern Pacific, Atlantic, and Indian Ocean regions are shown in percent. Temperature profile changes (lower row) for the four tropical regions are in K. Small triangles along the bottom axes indicate the retrieved SST change for each season.

Table 1. Number of Total Spectra, Number of Clear Spectra, Brightness Temperature Threshold (BTT), and Observed Mean SST for Each Geographic Region.

	WP	EP	AT	IN	AFN	AFD	NP	NA
XAM 1970								
Total	1566	1505	668	1034	480	560	2092	1094
Clear	569	762	271	304	402	375	371	332
BTT, K	295.0	294.0	292.0	296.0	273.0	300.0	274.0	279.0
Ts (obs)*, K	301.9	299.9	301.0	302.8	-	-	280.6	285.7
JJA 1970								
Total	2332	2350	701	1602	826	898	3463	1600
Clear	1181	1112	379	443	724	805	550	426
BTT, K	295.0	292.0	292.0	293.0	281.0	304.0	283.0	286.0
Ts (obs)*, K	301.5	297.4	298.4	301.1	-	-	285.5	290.1
SON 1970								
Total	2177	2166	547	1493	341	867	3171	1625
Clear	1288	994	181	510	217	433	418	245
BTT, K	294.0	291.0	293.0	294.0	277.0	301.0	282.0	286.0
Ts (obs)*, K	301.0	296.7	298.8	300.9	-	-	286.6	289.3
DJX 1970-71								
Total	854	881	184	575	58	351	532	568
Clear	462	327	78	184	39	209	242	107
BTT, K	293.0	292.0	293.0	294.0	267.0	286.0	275.0	278.0
Ts (obs)*, K	300.5	296.9	299.8	300.6	-	-	284.1	285.7

* Reynolds, [1988].

Table 2. Retrieved Changes in Ozone, Water Vapor (ΔW), and Temperature (ΔT) Parameters for the 1970 Seasonal Minus Annual Mean Spectral Radiance Differences in Figure 10.

	Equatorial Western Pacific (WP)				Equatorial Eastern Pacific (EP)			
Parameter	XAM-ANN	JJA-ANN	SON-ANN	DJX-ANN	XAM-ANN	JJA-ANN	SON-ANN	DJX-ANN
Δ Ozone, %	-0.062	0.074	-0.004	-0.075	-0.056	0.066	-0.024	0.021
ΔW/ΔZ, %	-3.91	1.40	0.533	-1.20	-4.54	3.73	1.89	-1.11
ΔW(column), %	9.05	2.22	-9.30	-2.63	4.29	4.07	-7.93	-10.2
ΔT/ΔZ, K/km	0.028	0.075	-0.061	-0.061	0.129	-0.011	-0.176	0.085
ΔT(layer), K	0.745	0.730	-0.569	-0.896	1.53	0.033	-1.85	0.046
ΔTs, K	1.04	0.446	-0.445	-1.15	1.61	-0.06	-1.45	-0.697
ΔTs(obs)*, K	0.71	0.23	-0.20	-0.77	2.29	-0.21	-0.88	-0.66
VR	0.691	0.154	0.301	0.331	0.715	0.147	0.500	0.524

* Reynolds, [1988].

Table 3. Retrieved Changes in Ozone, Water Vapor (ΔW), and Temperature (ΔT) Parameters for the 1970 Seasonal Minus Annual Mean Spectral Radiance Differences in Figure 11.

	Equatorial Atlantic Ocean (AT)				Equatorial Indian Ocean (IN)			
Parameter	XAM-ANN	JJA-ANN	SON-ANN	DJX-ANN	XAM-ANN	JJA-ANN	SON-ANN	DJX-ANN
Δ Ozone, %	-0.138	0.066	0.041	0.109	0.059	-0.004	-0.028	0.007
ΔW/ΔZ, %	-1.38	0.959	0.501	-0.472	3.23	1.24	-1.90	-2.00
ΔW(column), %	16.4	-8.03	-7.60	0.532	21.4	12.3	-21.6	-12.7
ΔT/ΔZ, K/km	0.036	0.010	-0.076	0.146	0.138	0.202	-0.209	-0.095
ΔT(layer), K	0.294	0.150	-0.490	0.834	1.91	1.17	-1.72	-0.802
ΔTs, K	0.861	-0.581	-0.015	0.968	2.02	-0.925	-0.516	-0.757
ΔTs(obs)*, K	1.12	-0.59	-0.36	0.31	0.99	-0.10	-0.26	-0.44
VR	0.726	0.343	0.465	0.800	0.545	0.721	0.490	0.581

* Reynolds, [1988].

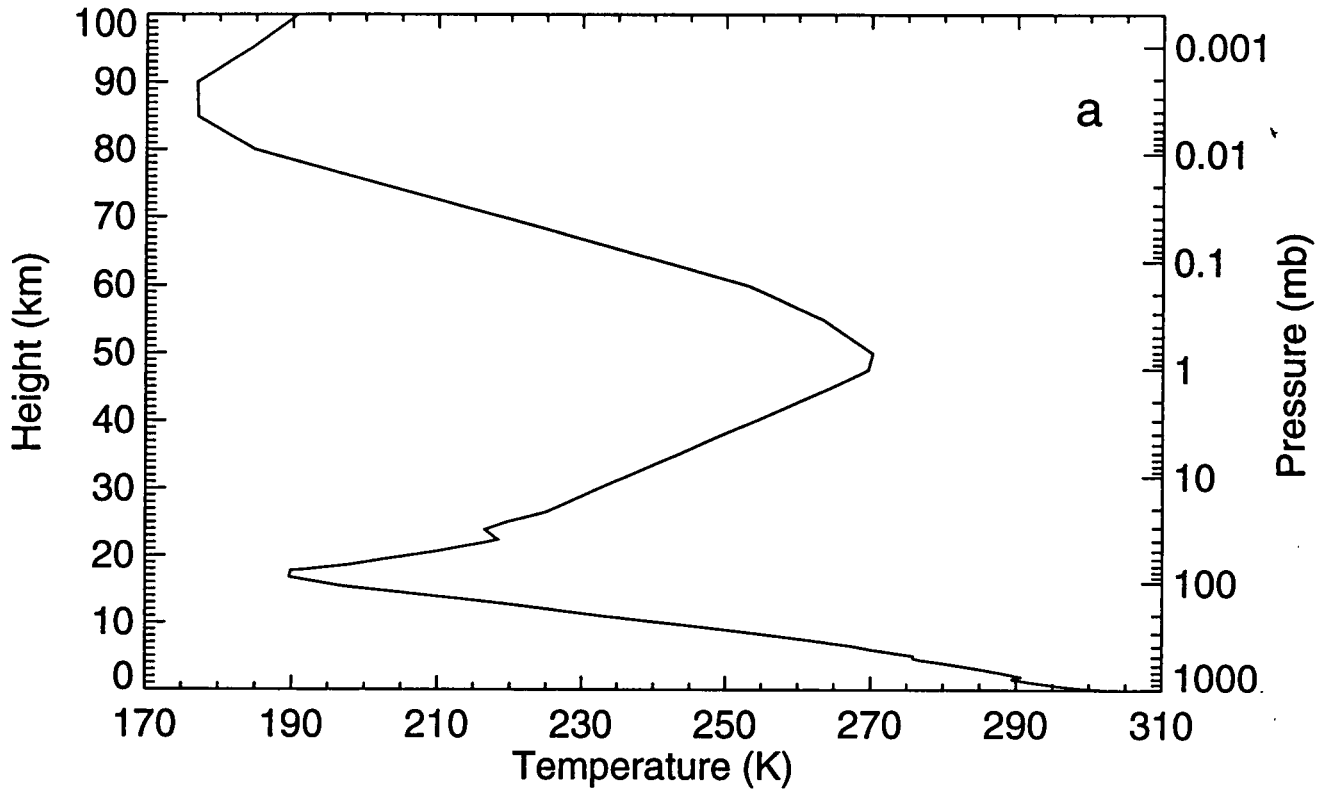
a
Height (km)
Pressure (mb)
Temperature (K)
100
90
80
70
60
50
40
30
20
10
0
0.001
0.01
0.1
1
10
100
1000
170
190
210
230
250
270
290
310

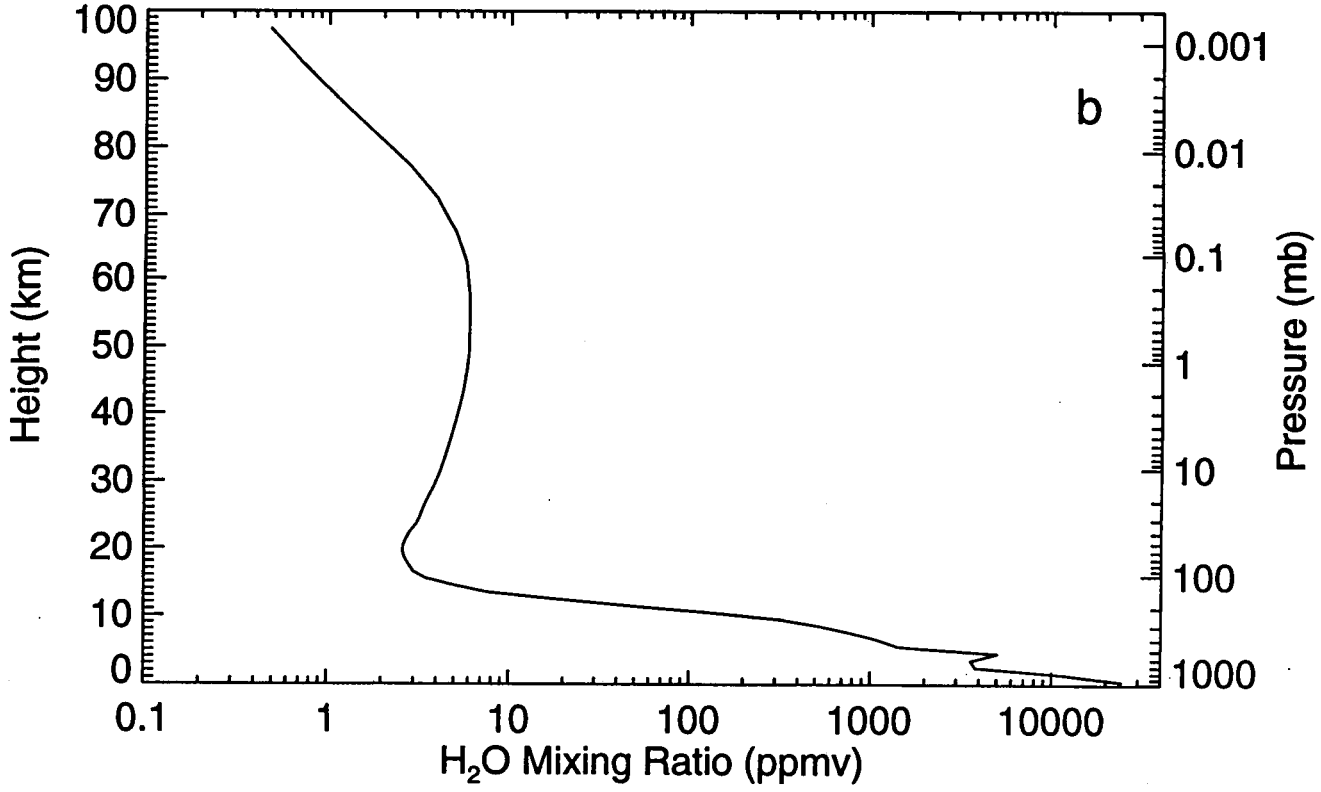
b
Height (km)
Pressure (mb)
H_2O Mixing Ratio (ppmv)
100
90
80
70
60
50
40
30
20
10
0
0.001
0.01
0.1
1
10
100
1000
0.1
1
10
100
1000
10000

FIGURE 1

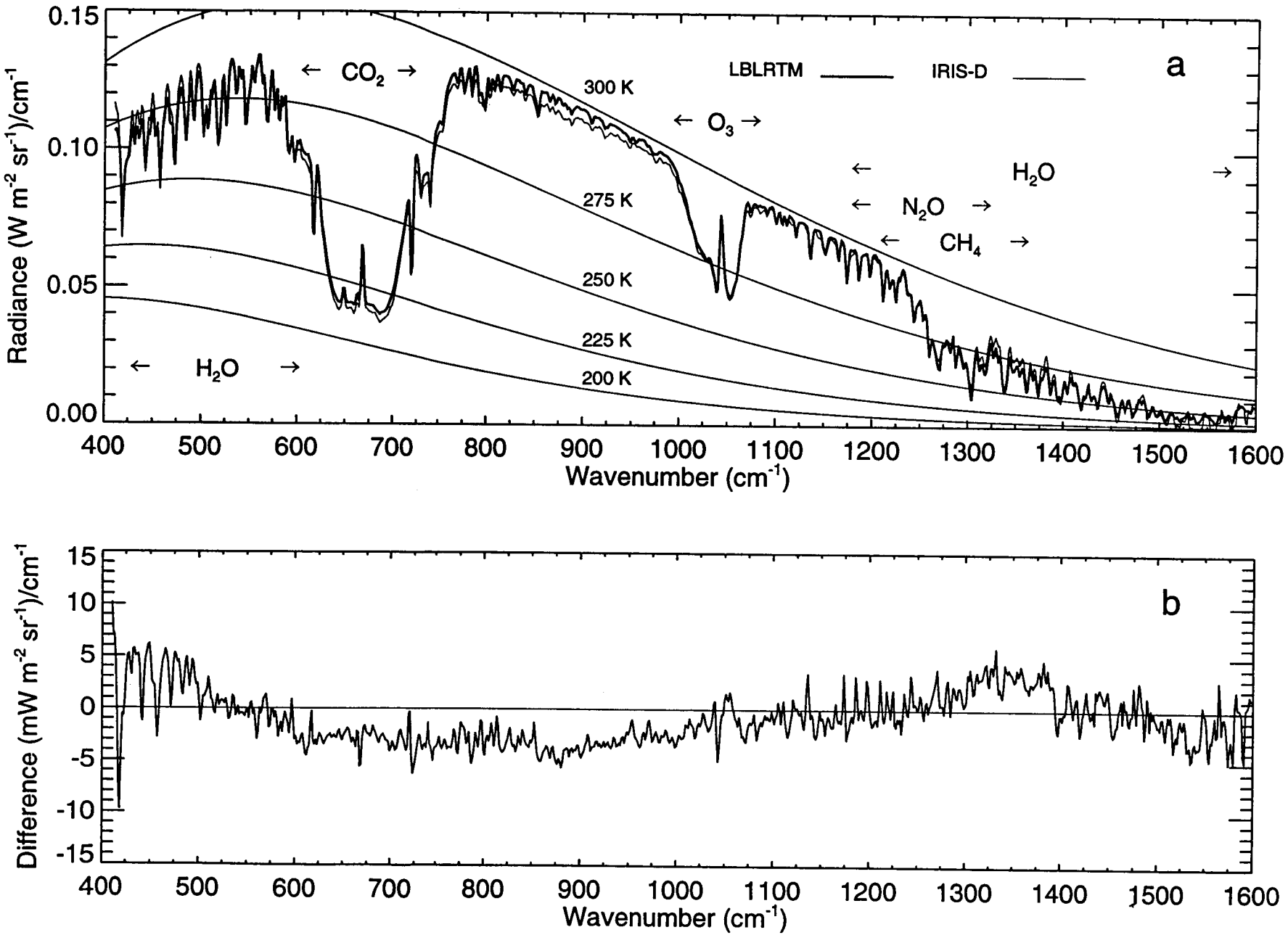
a
LBLRTM
IRIS-D
300 K
275 K
250 K
225 K
200 K
← CO2 →
← O3 →
← H2O →
← N2O →
← CH4 →
← H2O →
Radiance (W m-2 sr-1)/cm-1
Wavenumber (cm-1)
b
Difference (mW m-2 sr-1)/cm-1
Wavenumber (cm-1)

FIGURE 2 a-b

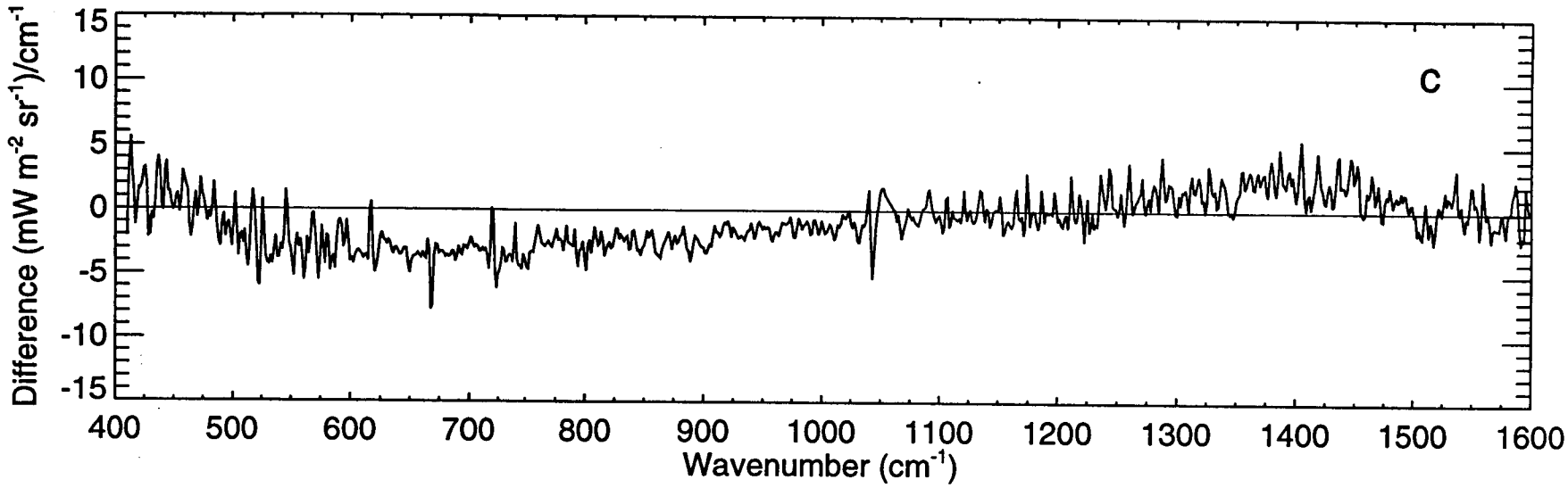
c
Difference (mW m-2 sr-1)/cm-1
15
10
5
0
-5
-10
-15
400
500
600
700
800
900
1000
1100
1200
1300
1400
1500
1600
Wavenumber (cm-1)

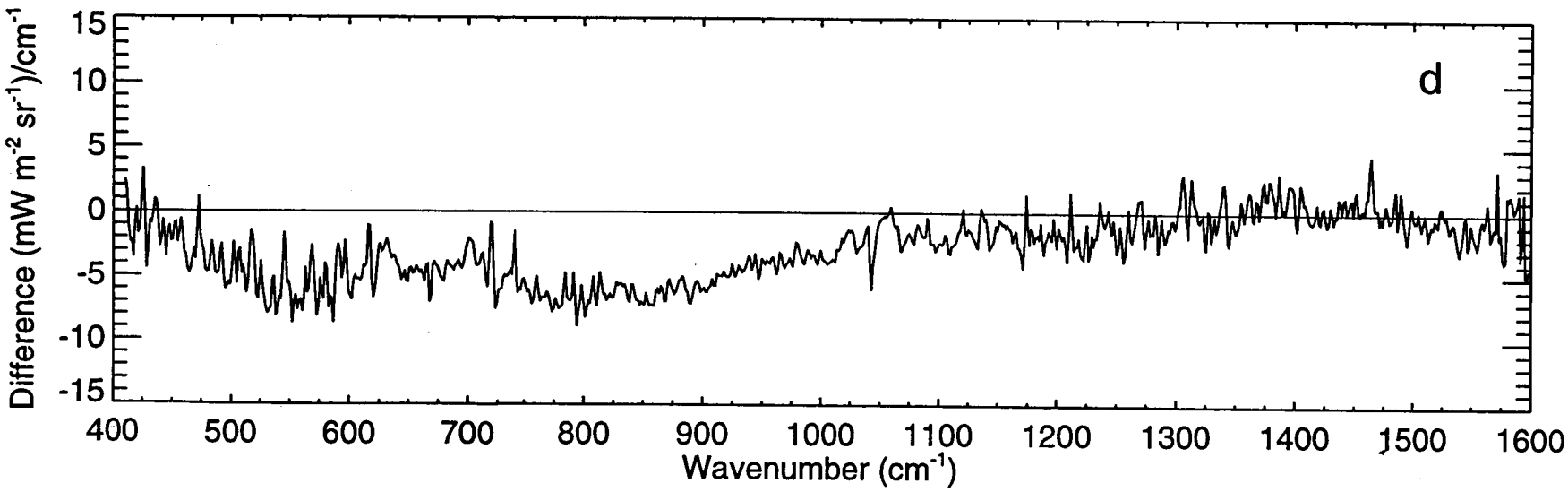
d
Difference (mW m-2 sr-1)/cm-1
15
10
5
0
-5
-10
-15
400
500
600
700
800
900
1000
1100
1200
1300
1400
1500
1600
Wavenumber (cm-1)

FIGURE 2c-d

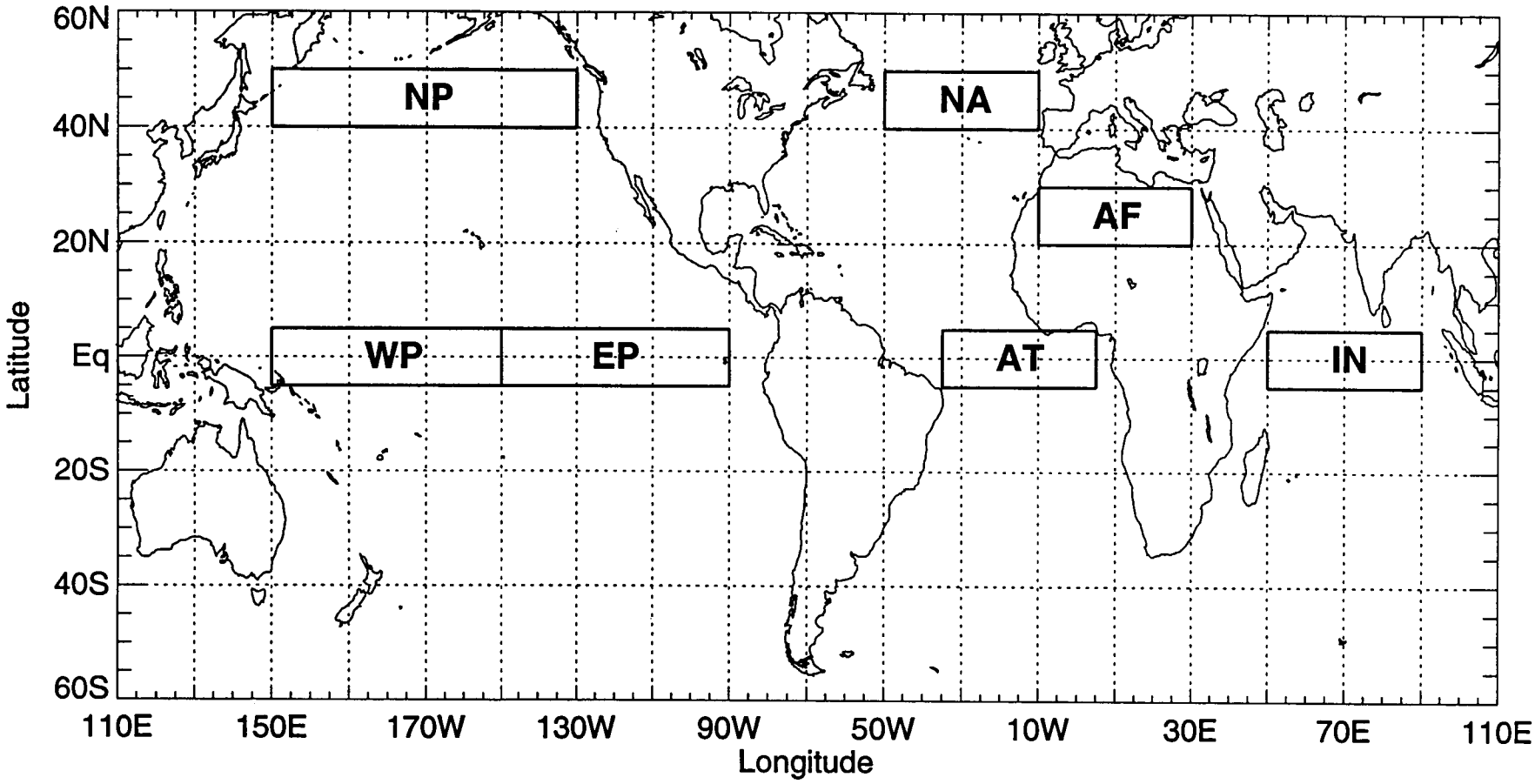
60N
40N
20N
Eq
20S
40S
60S
Latitude
110E
150E
170W
130W
90W
50W
10W
30E
70E
110E
Longitude
NP
NA
AF
WP
EP
AT
IN

FIGURE 3

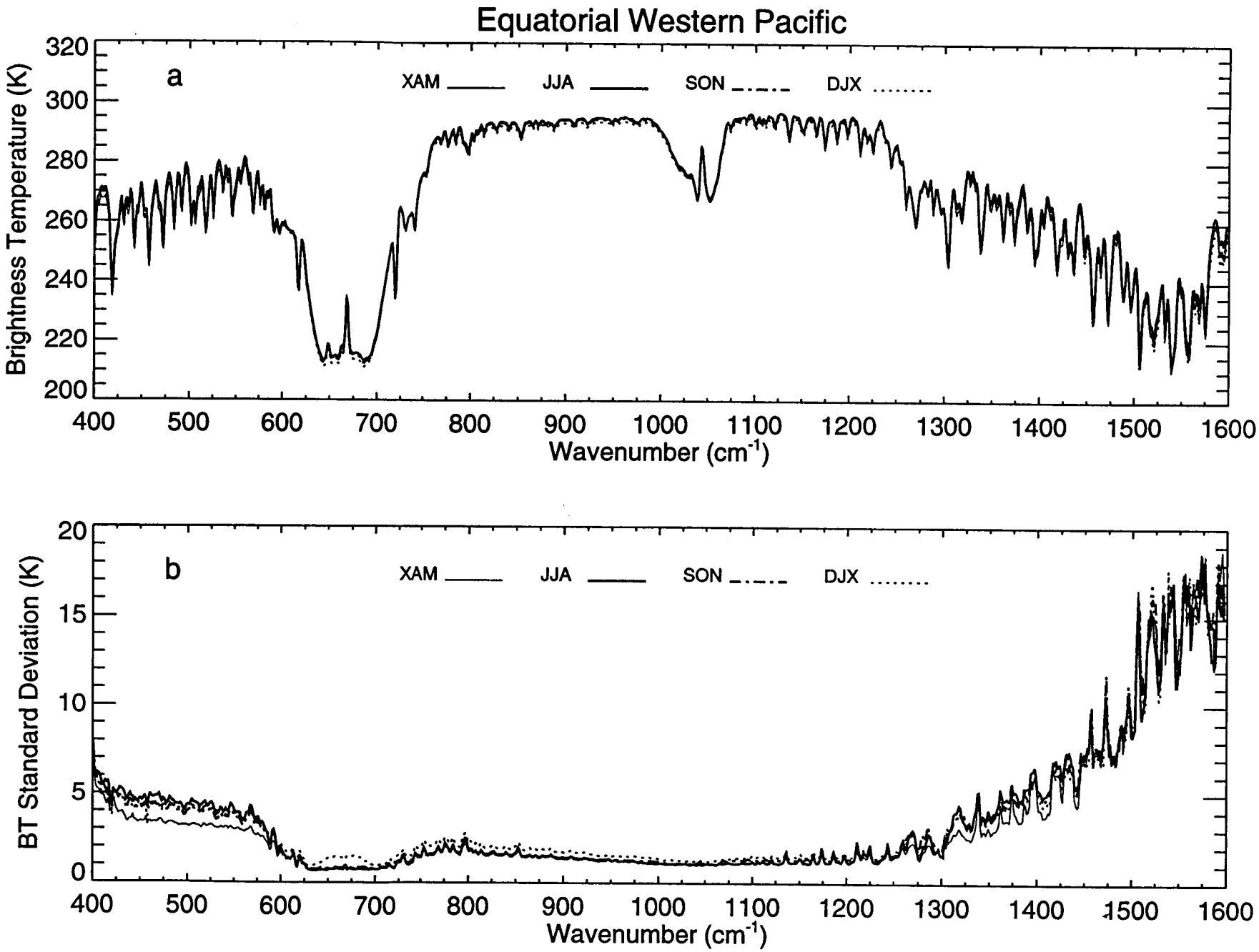
Equatorial Western Pacific
a
XAM
JJA
SON
DJX
Brightness Temperature (K)
320
300
280
260
240
220
200
400
500
600
700
800
900
1000
1100
1200
1300
1400
1500
1600
Wavenumber (cm-1)
b
XAM
JJA
SON
DJX
BT Standard Deviation (K)
20
15
10
5
0
400
500
600
700
800
900
1000
1100
1200
1300
1400
1500
1600
Wavenumber (cm-1)

FIGURE 4

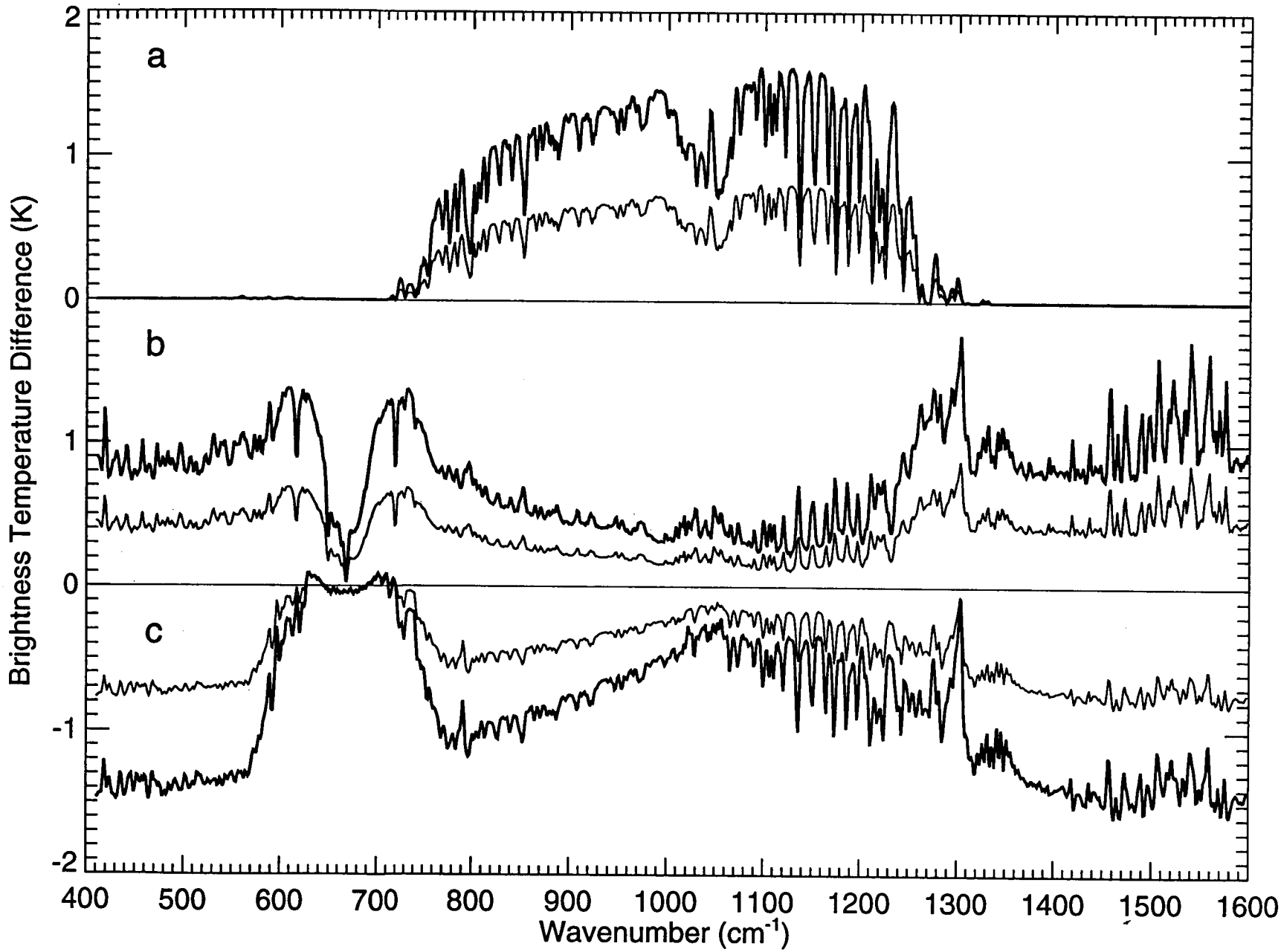
a
b
c
Brightness Temperature Difference (K)
2
1
0
1
0
-1
-2
400
500
600
700
800
900
1000
1100
1200
1300
1400
1500
1600
Wavenumber (cm-1)

FIGURE 5

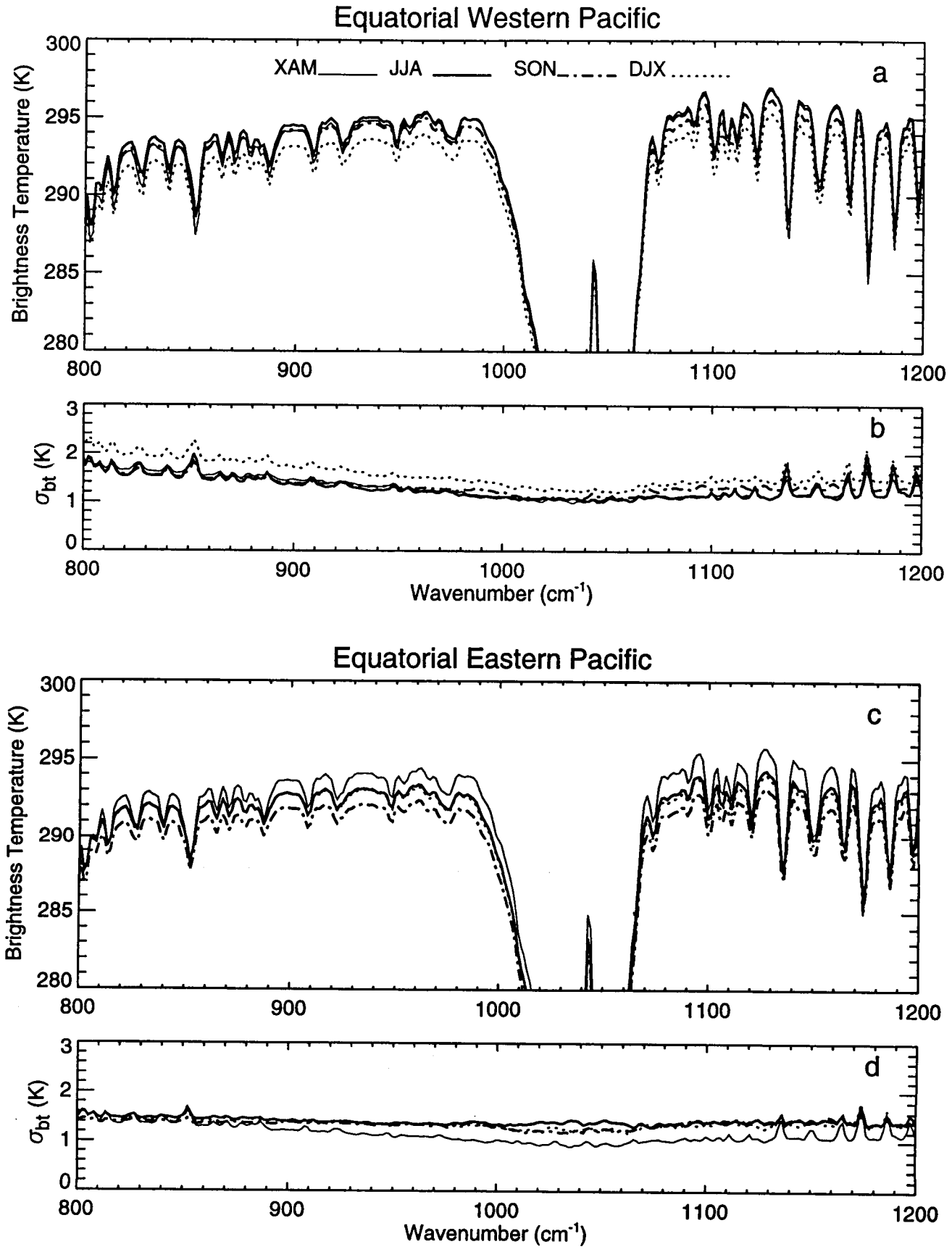
Equatorial Western Pacific
XAM
JJA
SON
DJX
a
b
Brightness Temperature (K)
σ_{bt} (K)
Wavenumber (cm^{-1})
Equatorial Eastern Pacific
c
d
Brightness Temperature (K)
σ_{bt} (K)
Wavenumber (cm^{-1})

FIGURE 6

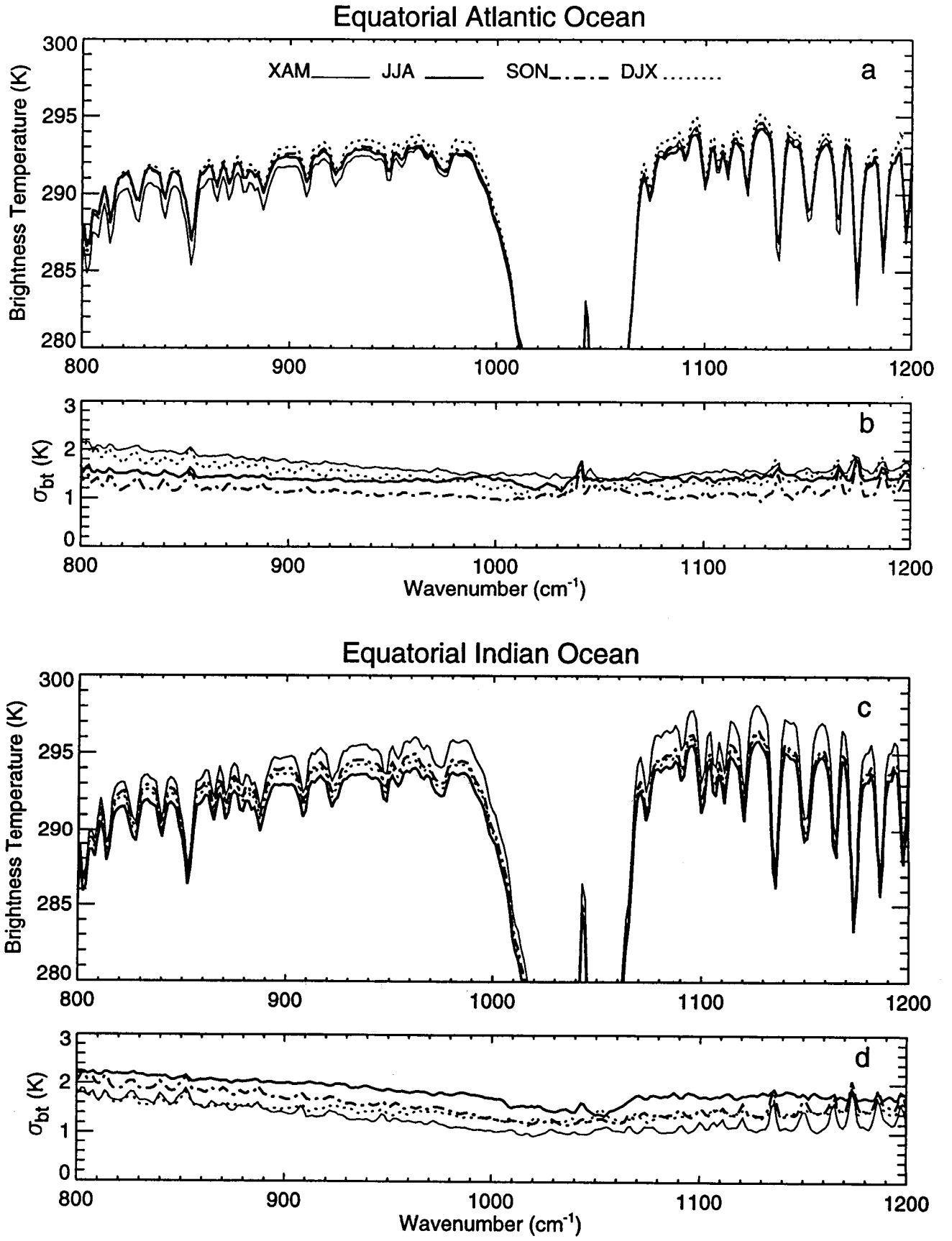
Equatorial Atlantic Ocean
XAM
JJA
SON
DJX
a
b
Brightness Temperature (K)
σ_{bt} (K)
Wavenumber (cm^{-1})
Equatorial Indian Ocean
c
d
Brightness Temperature (K)
σ_{bt} (K)
Wavenumber (cm^{-1})

FIGURE 7

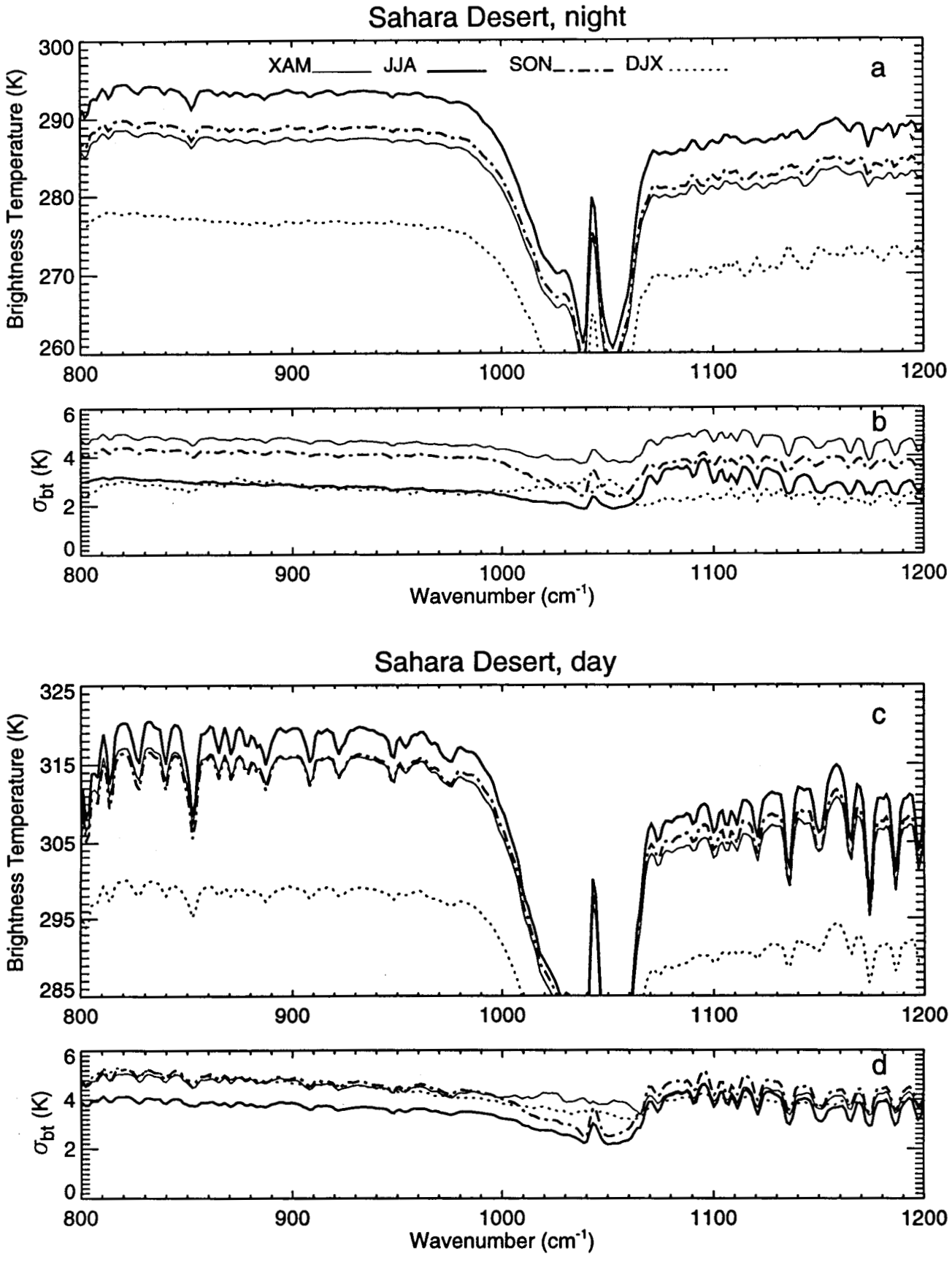
Sahara Desert, night
XAM
JJA
SON
DJX
a
b
Brightness Temperature (K)
σ_{bt} (K)
Wavenumber (cm^{-1})
Sahara Desert, day
c
d
Brightness Temperature (K)
σ_{bt} (K)
Wavenumber (cm^{-1})

FIGURE 8

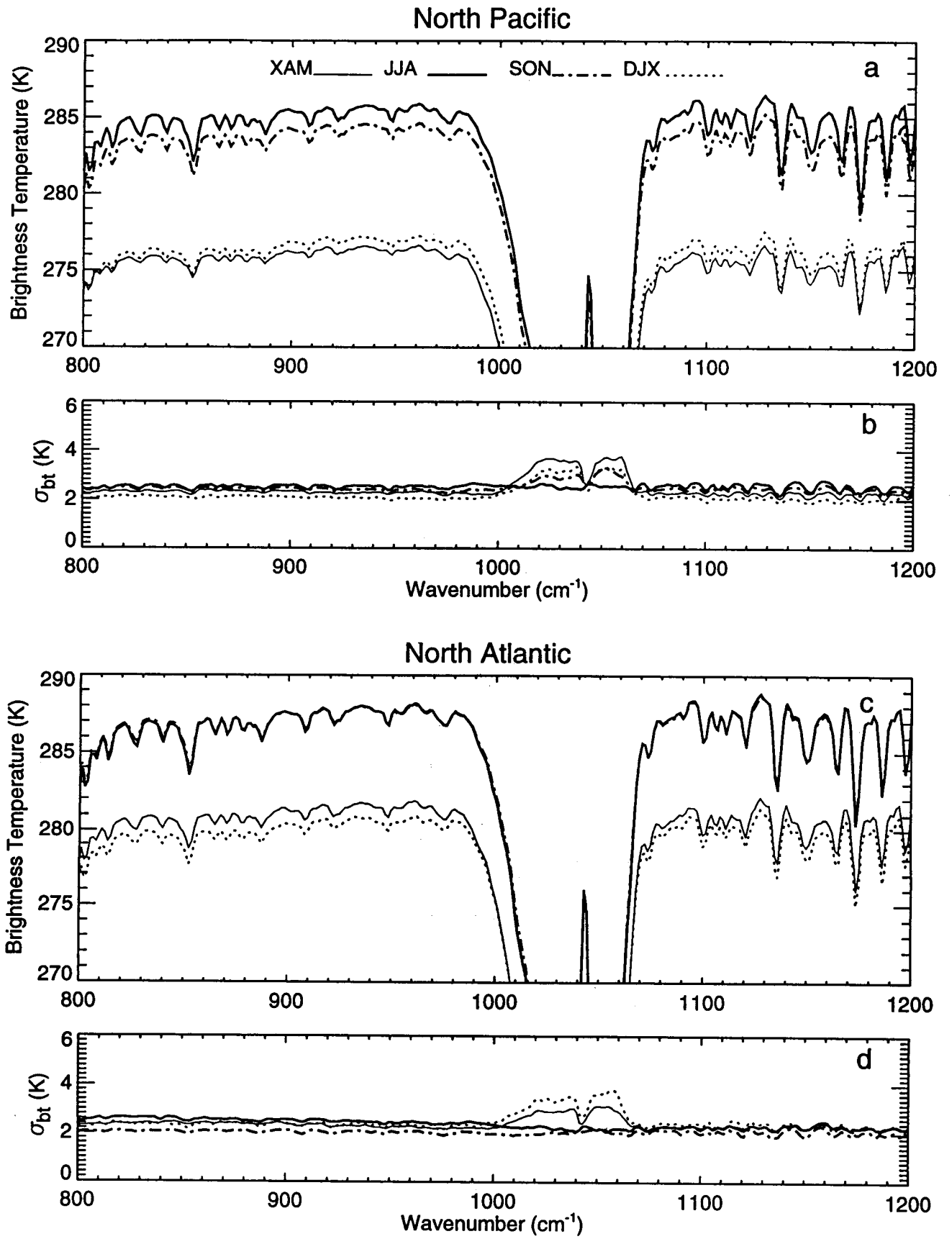
North Pacific
XAM
JJA
SON
DJX
a
b
Brightness Temperature (K)
σ_{bt} (K)
Wavenumber (cm^{-1})
North Atlantic
c
d
Brightness Temperature (K)
σ_{bt} (K)
Wavenumber (cm^{-1})

FIGURE 9

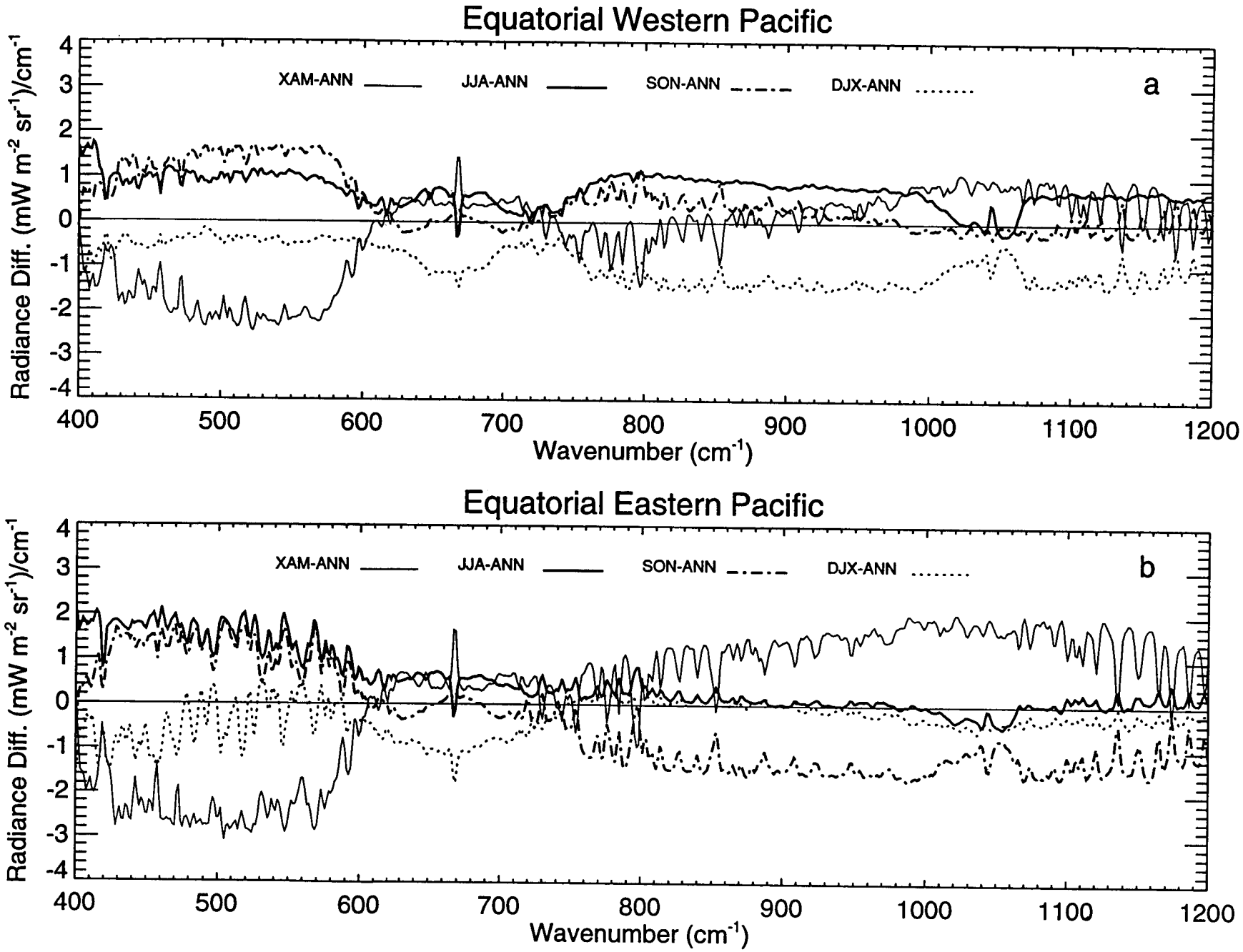
Equatorial Western Pacific
XAM-ANN
JJA-ANN
SON-ANN
DJX-ANN
a
Radiance Diff. (mW m-2 sr-1)/cm-1
Wavenumber (cm-1)
Equatorial Eastern Pacific
XAM-ANN
JJA-ANN
SON-ANN
DJX-ANN
b
Radiance Diff. (mW m-2 sr-1)/cm-1
Wavenumber (cm-1)

FIGURE 10

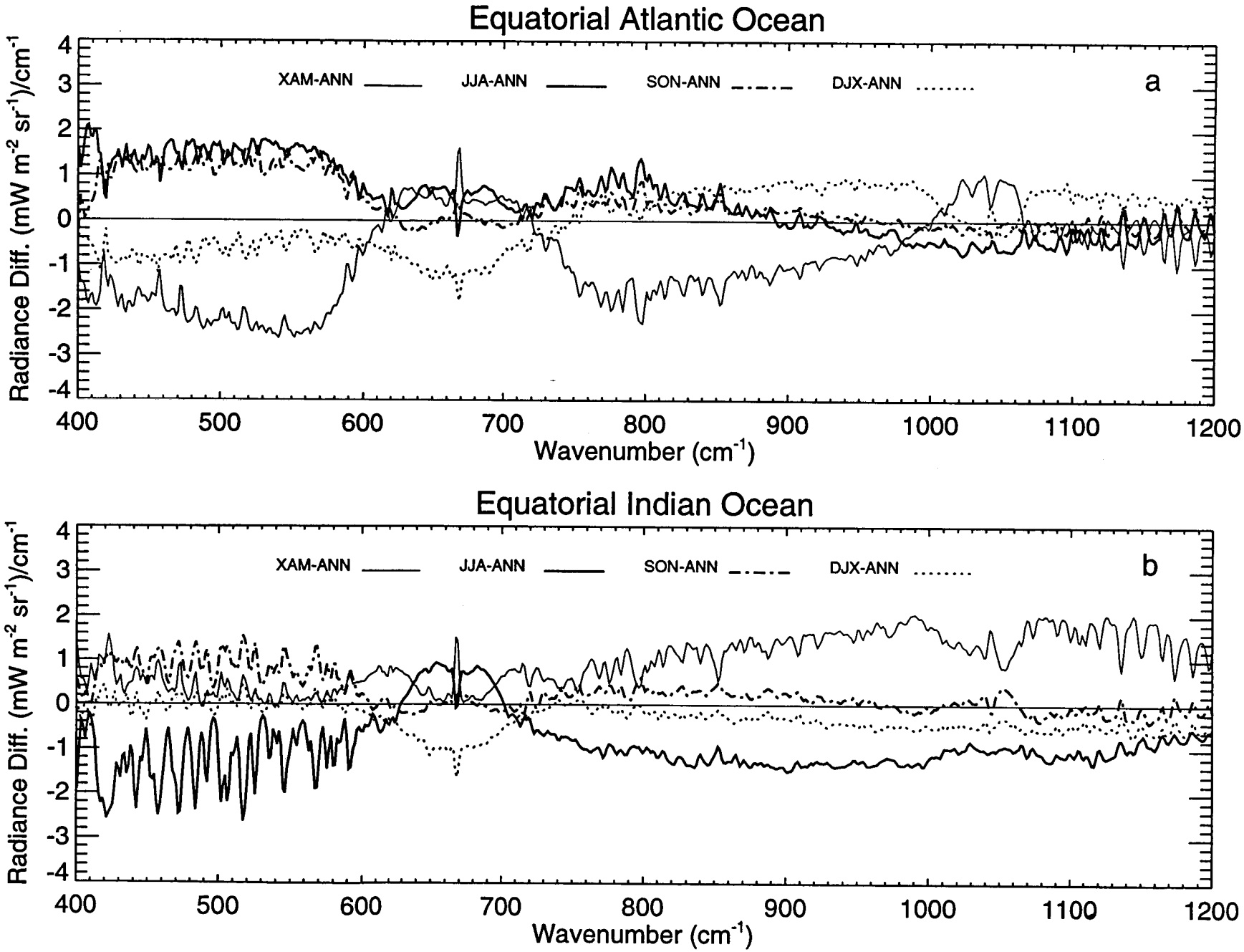
Equatorial Atlantic Ocean
XAM-ANN
JJA-ANN
SON-ANN
DJX-ANN
a
Radiance Diff. (mW m-2 sr-1)/cm-1
Wavenumber (cm-1)
Equatorial Indian Ocean
XAM-ANN
JJA-ANN
SON-ANN
DJX-ANN
b
Radiance Diff. (mW m-2 sr-1)/cm-1
Wavenumber (cm-1)

FIGURE 11

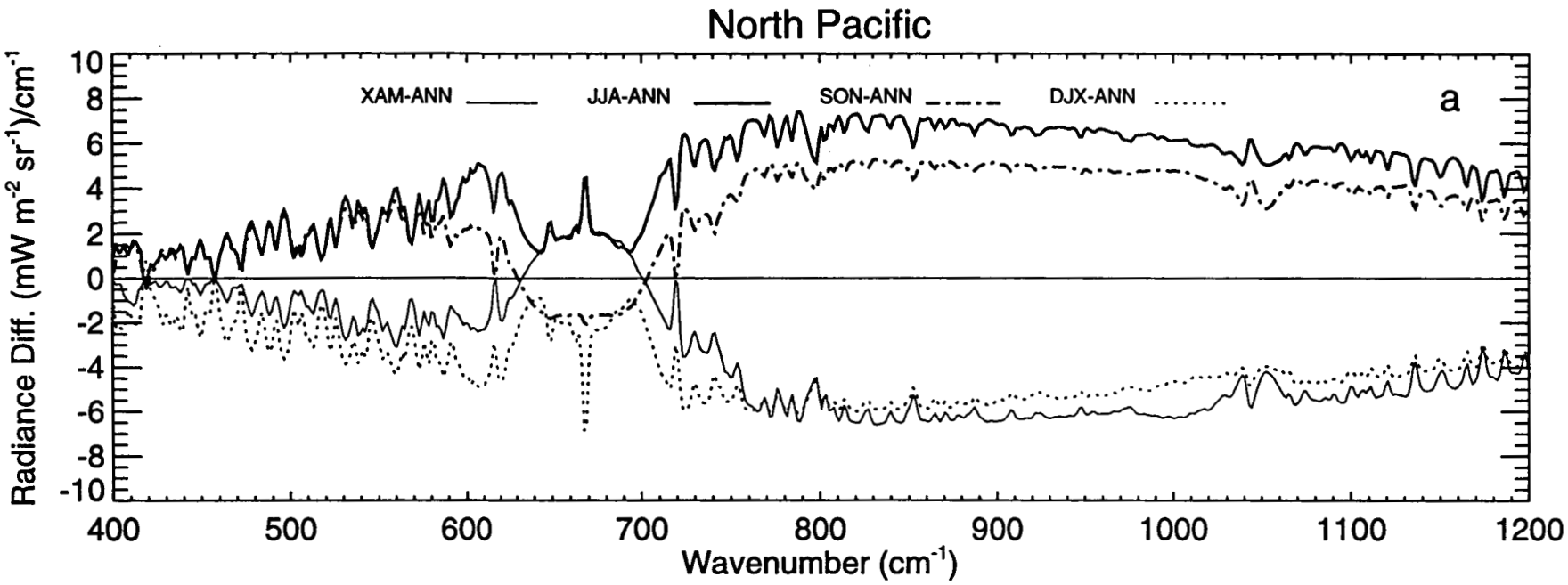
North Pacific
XAM-ANN
JJA-ANN
SON-ANN
DJX-ANN
a
Radiance Diff. (mW m-2 sr-1)/cm-1
Wavenumber (cm-1)
10
8
6
4
2
0
-2
-4
-6
-8
-10
400
500
600
700
800
900
1000
1100
1200

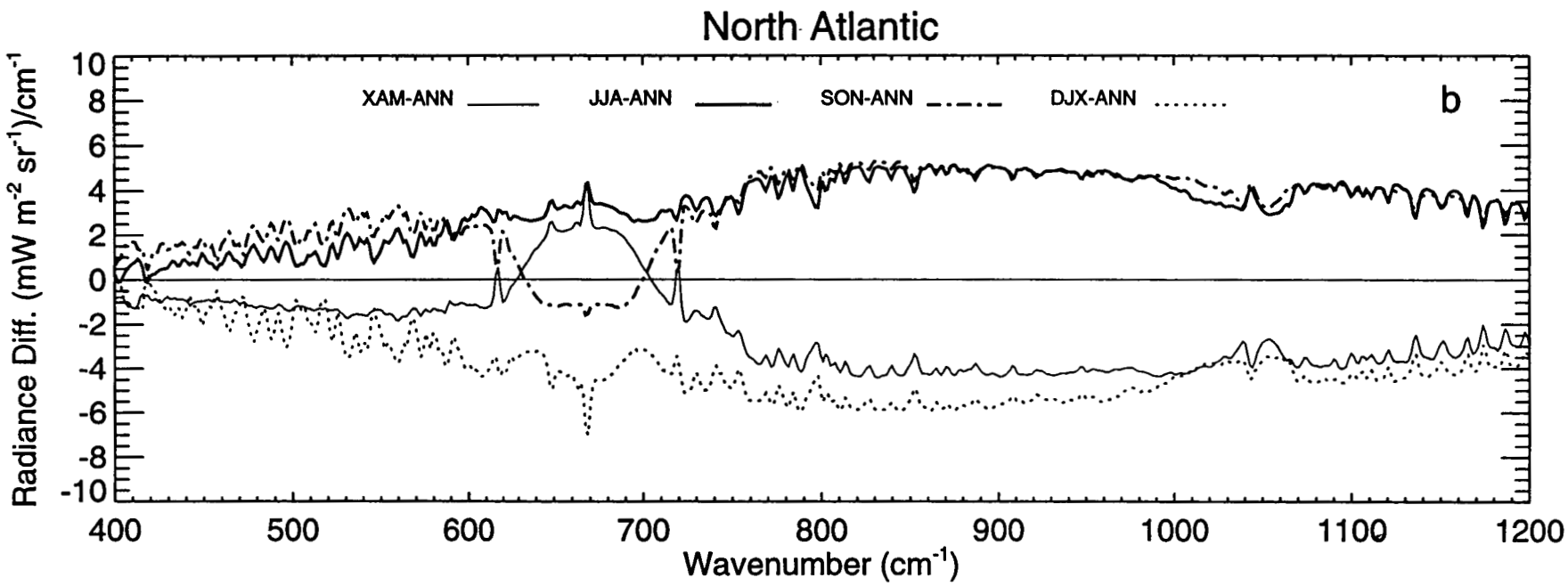
North Atlantic
XAM-ANN
JJA-ANN
SON-ANN
DJX-ANN
b
Radiance Diff. (mW m-2 sr-1)/cm-1
Wavenumber (cm-1)
10
8
6
4
2
0
-2
-4
-6
-8
-10
400
500
600
700
800
900
1000
1100
1200

FIGURE 12

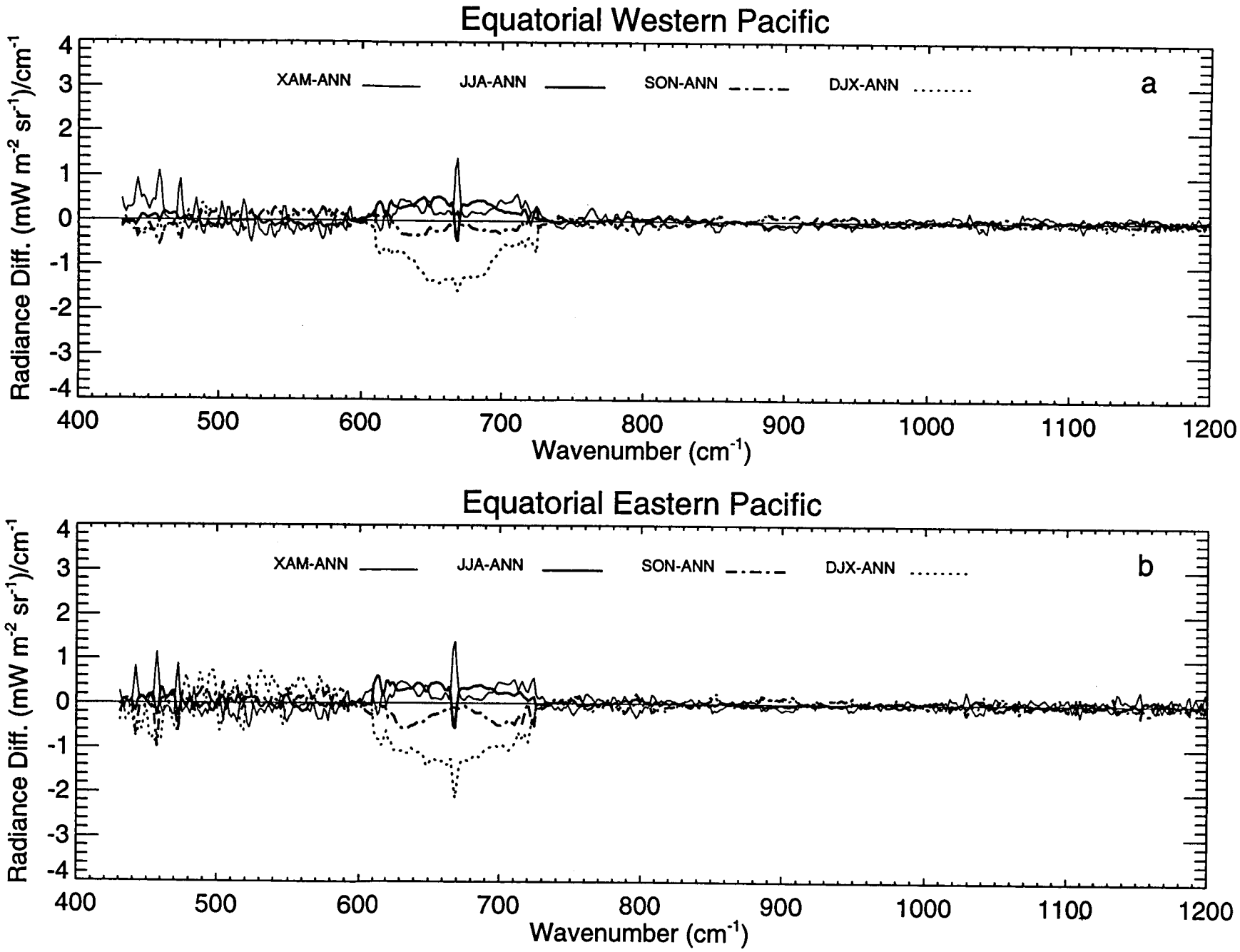
Equatorial Western Pacific
XAM-ANN
JJA-ANN
SON-ANN
DJX-ANN
a
Radiance Diff. (mW m-2 sr-1)/cm-1
Wavenumber (cm-1)
Equatorial Eastern Pacific
XAM-ANN
JJA-ANN
SON-ANN
DJX-ANN
b
Radiance Diff. (mW m-2 sr-1)/cm-1
Wavenumber (cm-1)

FIGURE 13

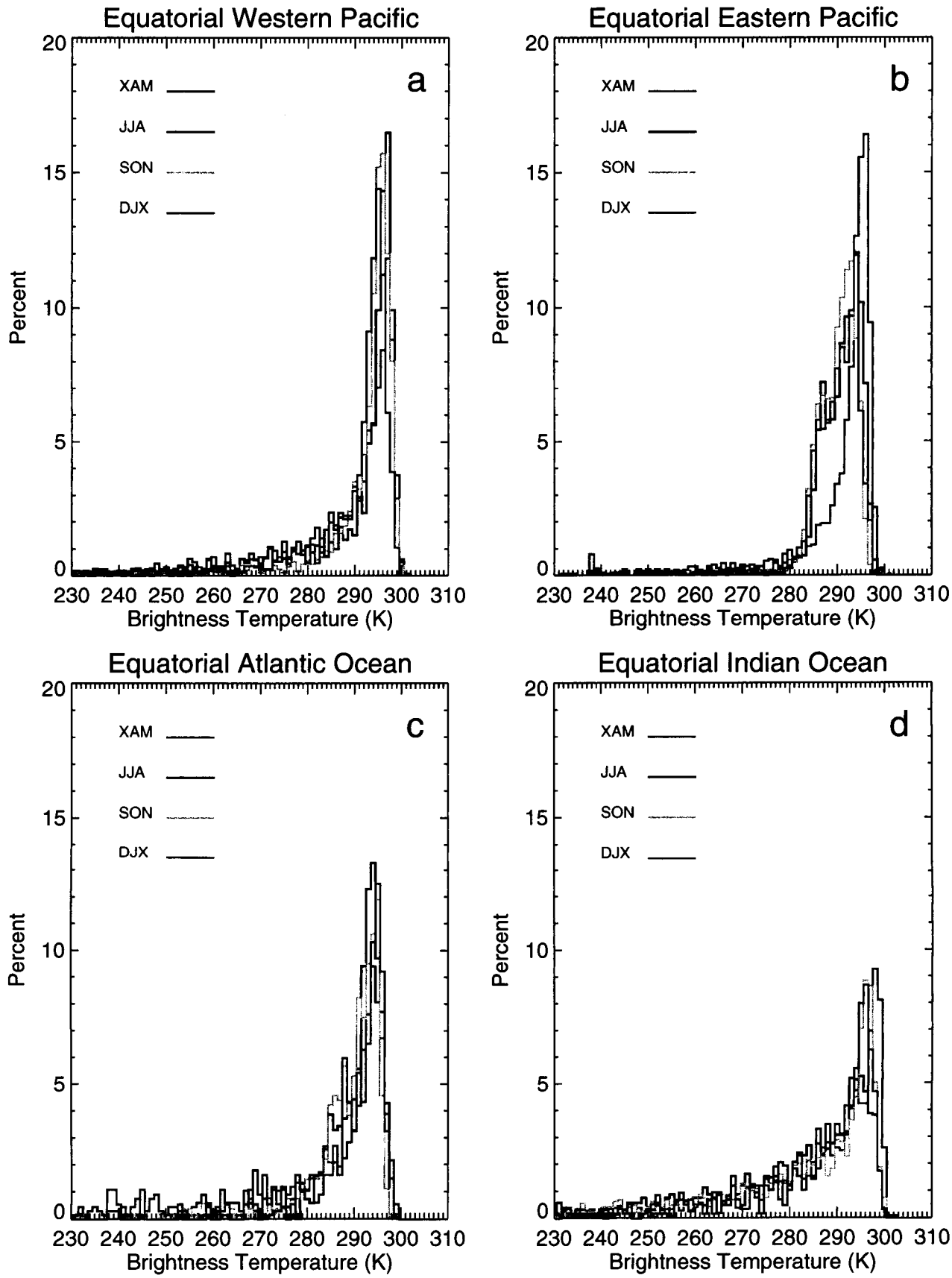
Equatorial Western Pacific
a
XAM
JJA
SON
DJX
Percent
Brightness Temperature (K)
Equatorial Eastern Pacific
b
XAM
JJA
SON
DJX
Percent
Brightness Temperature (K)
Equatorial Atlantic Ocean
c
XAM
JJA
SON
DJX
Percent
Brightness Temperature (K)
Equatorial Indian Ocean
d
XAM
JJA
SON
DJX
Percent
Brightness Temperature (K)

PLATE 1

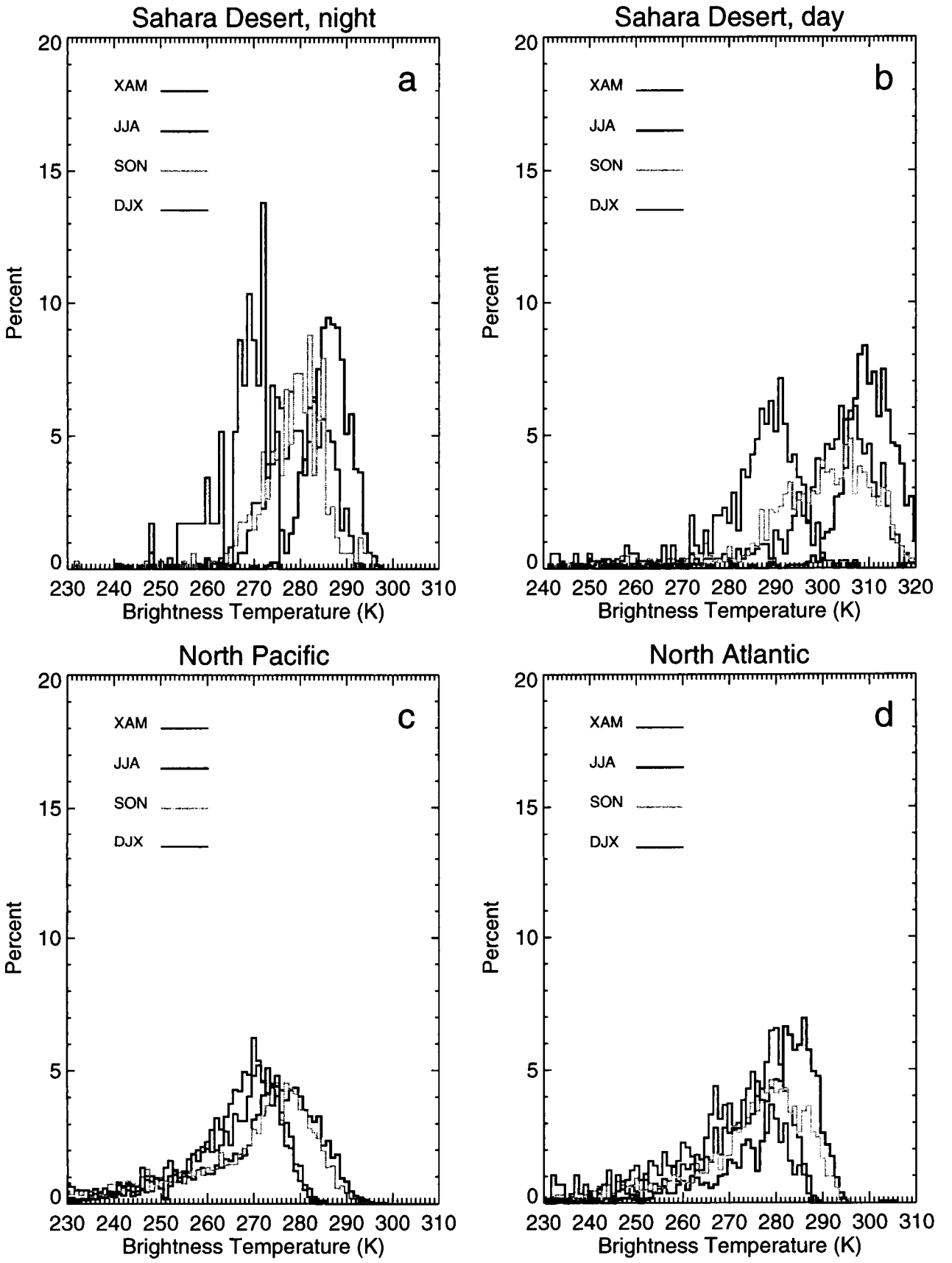
Sahara Desert, night
a
XAM
JJA
SON
DJX
Percent
Brightness Temperature (K)
Sahara Desert, day
b
XAM
JJA
SON
DJX
Percent
Brightness Temperature (K)
North Pacific
c
XAM
JJA
SON
DJX
Percent
Brightness Temperature (K)
North Atlantic
d
XAM
JJA
SON
DJX
Percent
Brightness Temperature (K)

PLATE 2

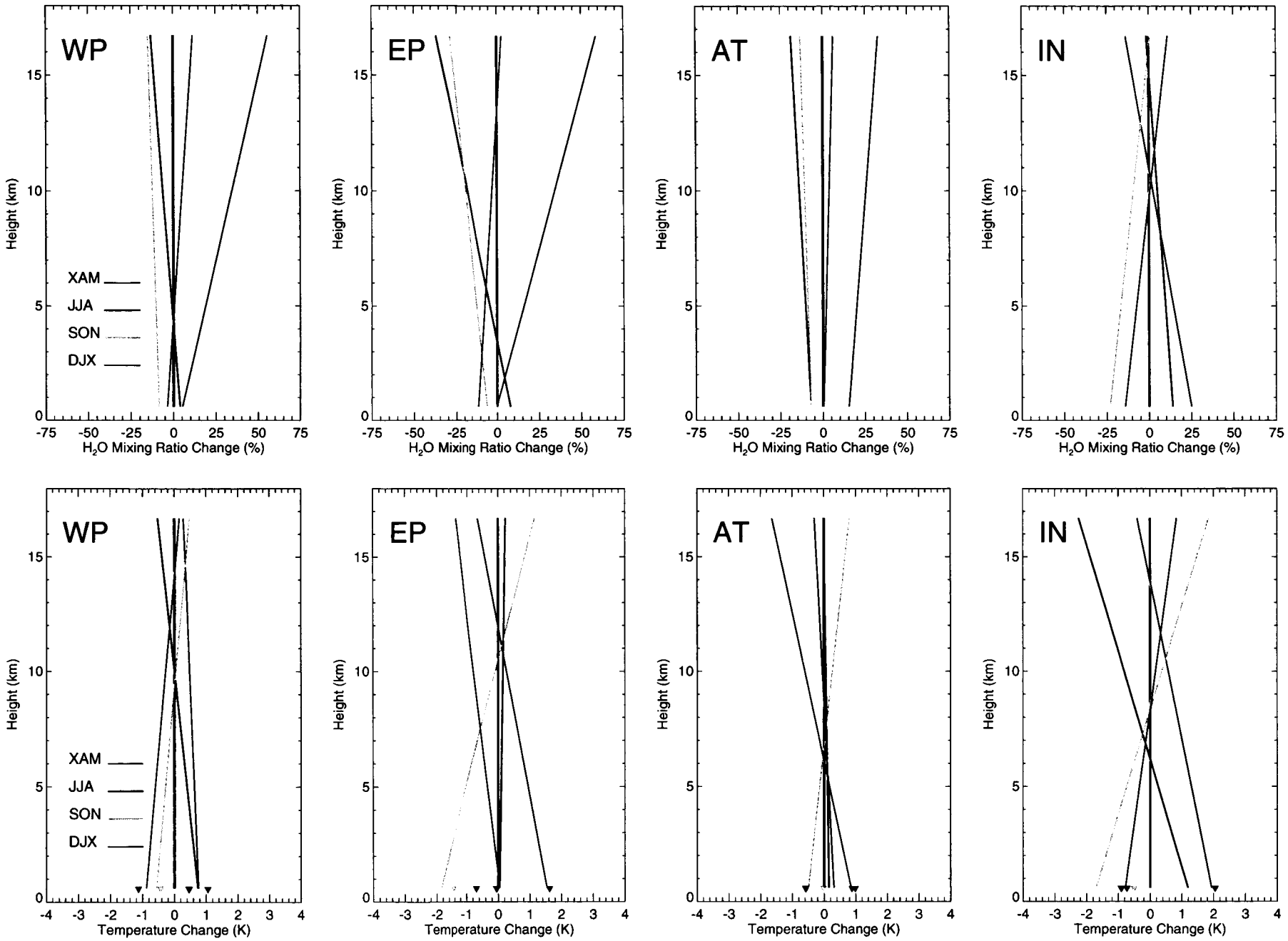
WP
EP
AT
IN
XAM
JJA
SON
DJX
Height (km)
H_2O Mixing Ratio Change (%)
Temperature Change (K)

PLATE 3

REPORT DOCUMENTATION PAGE

OMB No. 0704-0188

Public reporting burden for this collection of information is estimated to average 1 hour per response, including the time for reviewing instructions, searching existing data sources, gathering and maintaining the data needed, and completing and reviewing the collection of information. Send comments regarding this burden estimate or any other aspect of this collection of information, including suggestions for reducing this burden, to Washington Headquarters Services, Directorate for Information Operations and Reports, 1215 Jefferson Davis Highway, Suite 1204, Arlington, VA 22202-4302, and to the Office of Management and Budget, Paperwork Reduction Project (0704-0188), Washington, DC 20503.

1. AGENCY USE ONLY (Leave blank)	2. REPORT DATE	3. REPORT TYPE AND DATES COVERED
	27 March 1996	Final Report 1 Oct. 92 - 31 Mar. 96

4. TITLE AND SUBTITLE

Outgoing Spectral Radiance: A Climate Diagnostic

5. FUNDING NUMBERS

NASW-4752

6. AUTHOR(S)

Shepard A. Clough, Michael J. Iacono

7. PERFORMING ORGANIZATION NAME(S) AND ADDRESS(ES)

Atmospheric and Environmental Research, Inc.
840 Memorial Drive
Cambridge, MA 02139

8. PERFORMING ORGANIZATION REPORT NUMBER

P427

9. SPONSORING/MONITORING AGENCY NAME(S) AND ADDRESS(ES)

NASA Headquarters
Headquarters Contract Division
Washington, DC 20546

10. SPONSORING/MONITORING AGENCY REPORT NUMBER

11. SUPPLEMENTARY NOTES

12a. DISTRIBUTION/AVAILABILITY STATEMENT

12b. DISTRIBUTION CODE

13. ABSTRACT *(Maximum 200 words)*

14. SUBJECT TERMS

15. NUMBER OF PAGES

2

16. PRICE CODE

17. SECURITY CLASSIFICATION OF REPORT	18. SECURITY CLASSIFICATION OF THIS PAGE	19. SECURITY CLASSIFICATION OF ABSTRACT	20. LIMITATION OF ABSTRACT
Unclassified	Unclassified	Unclassified	